NOVA SCHOOL OF SCIENCE & TECHNOLOGY

DEPARTMENT OF PHYSICS

DANIEL BERBEREIA CARDOSO

BSc in Biomedical Engineering

WILSON'S DISEASE DIAGNOSTIC USING LASER-INDUCED GRAPHENE ELECTRODES FOR COPPER DETECTION

MASTER IN BIOMEDICAL ENGINEERING

NOVA University Lisbon

september, 2023

NOVA SCHOOL OF SCIENCE & TECHNOLOGY

DEPARTMENT OF PHYSICS

WILSON'S DISEASE DIAGNOSTIC USING LASER-INDUCED GRAPHENE ELECTRODES FOR COPPER DETECTION

DANIEL BERBEREIA CARDOSO

BSc in Biomedical Engineering

Adviser: Henrique Vazão de Almeida
Researcher, NOVA University Lisbon, Cenimat|i3N, DCM, FCT-NOVA

Co-adviser: Arben Merkoçi
Full Professor and Director, Institut Català de Nanociencia i Nanotecnologia, Nanobioelectronics & Biosensors Group

Examination Committee

Chair: Célia Maria Reis Henriques
Associate Professor, FCT-NOVA

Rapporteur: Joana Sofia Pereira Neto
Doctorate Investigator, Centro de Investigação de Materiais (CENIMAT)

Adviser: Henrique Vazão de Almeida
Researcher, NOVA University Lisbon, Cenimat|i3N, DCM, FCT-NOVA

MASTER IN BIOMEDICAL ENGINEERING

NOVA University Lisbon
september, 2023

Wilson's Disease diagnostic using laser-induced graphene electrodes for copper detection

This document was created with the (pdf/Xe/Lua)LaTeX processor and the NOVAthesis template (v7.0.2) [1].

To my parents,
I would like to express my deepest gratitude for your love and support throughout my life. Your sacrifices and hardships have been the driving force behind my success, and I could not have achieved my goals without your guidance and encouragement.
Your dedication to providing me with everything I needed to succeed in college will never be forgotten. I am grateful for everything you have done for me. Thank you for being the best parents I could ask for.
With love and appreciation,
Daniel Cardoso

Acknowledgements

I would like to express my gratitude to my research supervisors, Dr. Henrique Vazão de Almeida at CENIMAT FCT-UNL and Dr. Giulio Rosati Senior PostDoctoral Reasercher at ICN2, for giving me the opportunity to work in this field of study and for their guidance throughout the course of this work, and to Dr. Arben Merkoçi ICREA Professor and Director of Nanobioelectronics & Biosensors Group at ICN2 BIST Center, for giving me the opportunity to conduct research in his group and for providing me with invaluable laboratory experience.

I am very grateful to the Ph.D. students Tomás Pinto e Cruz de Oliveira Pinheiro and Massimo Urban, who taught me the methodology to conduct the research and to present the research as clearly as possible. It was a great privilege to work with them. Their patience, dynamism, motivation, friendship and sense of humor have been very welcome during the course of this project. They inspired me to always acheive my goals and aim higher.

I would like to express my sincere gratitude to the European EMERGE program for giving me the opportunity to carry out experiments in exchange laboratories under the best possible conditions. My time at the CENIMAT and ICN2 facilities was definitely a valuable experience. In addition, I am grateful to FCT-UNL and the Physics Department, which proved to be a wonderful place to expand my knowledge and make lifelong friendships.

A huge thank you to my parents and sister for their love, care, and support. For the sacrifices they have made for me over the years so that I could get the best education possible to prepare me for my future.

I would also like to thank my friends for their support, friendship and empathy.

”

“Hardships often prepare ordinary people for an extraordinary destiny.”

— C.S. Lewis

Abstract

Low-cost biosensors have become a prominent trend in healthcare due to their potential for providing affordable and accessible diagnostic tools. Wilson Disease is a rare genetic disorder that causes copper to accumulate in vital organs such as the brain and liver. Monitoring the copper levels in the body is crucial for the diagnosis and management of this disease that otherwise can be fatal. Wearable devices can offer a convenient and non-invasive method to monitor many biomarkers, including copper, which serves as a biomarker for Wilson Disease. Laser-induced graphene is a promising material for producing biosensors due to its low cost, high conductivity, and easy fabrication. In this project we idealized and tested the possibility of producing a wearable microfluidic biosensor that combines laser-induced graphene electrodes for the detection of heavy metals in body fluids such as sweat and urine with good sensitivity. The laser-induced graphene electrodes were produced using two eco-friendly substrates, Whatman 1 wax coated, and a double layered hydrophobic cellulose substrate supplied by AlmaScience. The electrode fabrication processed was optimized and a systematic study about its electrical, morphological, chemical, and electrochemical characteristics was carried out at CENIMAT, Lisbon. At ICN2, Barcelona, the electrochemical cell's heavy metal detection capabilities, more specifically copper, were tested using Square Wave Anodic Stripping Voltammetry to verify their potential for Wilson Disease's diagnostic. These tests started with a Drop Method, and Immersion Method setup where the electrode was tested in its normal form and with a countertop setup, respectively. The electrodes were later integrated in a detection system along with a laser fabricated and optimized microfluidics channel designed for detecting copper in the parts per billion range, which allows for the application of these electrodes in a compact and small wearable device. This prototype could be the beginning of a wearable device capable of daily monitoring copper levels in Wilson Disease patients with a Lower Limit of Detection and Sensitivity of 4.66 ppb and 0.0145 µA/ppb, respectively.

Resumo

Os biossensores de baixo custo tornaram-se uma tendência proeminente no ramo da saúde devido ao seu potencial para fornecer ferramentas de diagnóstico económicas e acessíveis. A Doença de Wilson é uma doença genética rara que provoca a acumulação de cobre em órgãos vitais como o cérebro e o fígado. A monitorização dos níveis de cobre no organismo é crucial para o diagnóstico e a gestão desta doença que, caso contrário, pode ser fatal. Os dispositivos portáteis podem oferecer um método cómodo e não invasivo para monitorizar muitos biomarcadores, incluindo o cobre, que serve como biomarcador da Doença de Wilson. O grafeno induzido a laser é um material promissor para a produção de biossensores devido ao seu baixo custo, alta condutividade e fácil fabrico. Neste projeto idealizámos e testámos a possibilidade de produzir um biossensor de microfluídica vestível que combina elétrodos de grafeno induzido por laser para a deteção de metais pesados em fluidos corporais como o suor e a urina, com boa sensibilidade. Os elétrodos de grafeno foram produzidos utilizando dois substratos ecológicos, Whatman 1 revestido a cera e um substrato de celulose hidrofóbica de dupla camada fornecido pela AlmaScience. O processo de fabrico dos elétrodos foi otimizado e foi efetuado um estudo sistemático das suas características elétricas, morfológicas, químicas e eletroquímicas no CENIMAT, Lisboa. No ICN2, em Barcelona, as capacidades de deteção de metais pesados da célula eletroquímica, mais especificamente o cobre, foram testadas utilizando a Voltametria de Decapagem Anódica de Onda Quadrada para verificar o seu potencial para o diagnóstico da Doença de Wilson. Estes testes começaram com uma configuração do Método da Gota e do Método da Imersão, em que o elétrodo foi testado na sua forma normal e com uma configuração de bancada, respetivamente. Posteriormente, os elétrodos foram integrados num sistema de deteção, juntamente com um canal de microfluídica otimizado e fabricado a laser, concebido para detetar cobre em volumes reduzidos, o que permite a aplicação destes elétrodos num dispositivo portátil compacto e pequeno. Este protótipo poderá ser o início de um dispositivo vestível capaz de monitorizar diariamente os níveis de cobre em doentes com Doença de Wilson com um Limite Inferior de Deteção e uma Sensibilidade de 4.66 ppb e 0.0145 µA/ppb, respetivamente.

Contents

List of Figures

List of Tables

Acronyms

AB	Acetate Buffer
C	Celsius
CE	Counter Electrode
CENIMAT	CENIMAT i3N - Centro de Investigação de Materiais (Lab. Associado I3N)
CV	Cyclic Voltammetry
CVD	Chemical Vapor Deposition
DLHC	double-layered hydrophobic cellulose
ECSA	Electrochemically Active Surface Area
FSS	fluid Heavy Metal sensing system
HM	Heavy Metals
Hz	Hertz
ICN2	Institut Català de Nanociència i Nanotecnologia
IDA	iminodiacetatic acid
Ip	peak current
IUPAC	International Union of Pure and Applied Chemistry
k^0	Heterogeneous Electron-transfer Rate Determination
LIG	Laser-induced graphene
LOD	Lower Limit of Detection
mTAS	micro total analysis system

NCC	Non-caeruloplasmin-bound copper
P	Power
PET	Polyethylene terephthalate
ppb	parts per billion
PPI	Points Per Inch
ppm	parts per million
PW	Pulse-width
RE	Reference Electrode
RGB	Red Green Blue
S	Speed
SEM	Scanning electron microscopy
SWASV	Square Wave Anodic Stripping Voltammetry
W	Watts
WD	Wilson Disease
WE	Working Electrode

1 Introduction

1.1 Context and Motivation

Wilson Disease (WD) is a rare disorder inherited by autosomal-recessive fashion and affects between 10 to 30 million individuals, 1 per 10,000 to 30,000 people worldwide according to the World Health Organization [2]. If both parents carry a defective gene for WD, there is a 25% chance in each pregnancy that the child will have the disorder [3].

This disease is characterized by the accumulation of copper throughout the body. Tissues such as the liver, brain, and eyes are the most affected and some of the symptoms include vomiting, ascites, swelling of the legs, tremors, muscle stiffness, personality changes, anxiety, and auditory or visual hallucinations [4]. One of the clearest symptoms of WD is the Kayser-Fleischer rings which can be seen around the cornea. Although not always visible, the Kayser-Fleischer ring is a distinguishing symptom of the illness. While only 50-60% of individuals without neurological symptoms and 10% of asymptomatic siblings exhibit this ring, 95% of patients with neurologic symptoms present it [5].

There has been a rise in health concerns associated with environmental contamination by Heavy Metals (HM). This problem has become more relevant in the last decades because of the exponential exposure humans have to these elements through industrial, agricultural, domestic, and technological applications [6].

The diagnosis of WD can be quite challenging. Patients with predominant neurological symptoms often experience delays in symptom manifestation, making it challenging for clinicians to screen for WD. Additionally, patients with unknown liver diseases may complicate the diagnosis [7].

The diagnostic of WD is usually made combining different tests, namely the Standard Tests and Urinary Copper Excretion tests [8]. The first is a general inspection of the medical personnel, to determine possible visual symptoms, like the Kayser-Fleischer rings, and monitor ceruloplasmin levels, protein that carries copper from the liver into the organs via bloodstream [9]. Although this might be an effective temporary screening, it fails in the case of patients who do not show visual symptoms or clear results. In that case urinary copper extraction is performed to confirm the diagnosis, within a 24-hour monitoring

window [10].

Typical therapies of the WD are life-long therapies, and usually include two phases, one being the actual therapy, along with drugs, and the second being a maintenance phase, with permanent changes in life style and diet. The gold standard treatment guidelines for WD all agree on the use of a chelating agent (penicillamine or trientene), but they disagree on the use of zinc for combination therapy in the initial therapy. This first stage requires at least a year to complete, and a low copper diet should also be put in place [11].

A stable clinical and biochemical condition as well as a balanced copper homeostasis are the main targets of long-term therapy for WD. Therefore, monitoring should include checking for patient compliance as well as looking for indicators of re-coppering or over-de-coppering. Although the frequency of monitoring varies on the patients level of impairment, it is advised to do a checkup once or twice a year [12]. The 24-hour urine copper and Non-caeruloplasmin-bound copper (NCC) are the two key measures of copper balance in the maintenance phase, according to all three of the various standards. Additionally, they all concur that the ideal range for daily urine copper excretion should be between 200 and 500 μg/day [11],[12].

In the majority of untreated individuals, NCC is raised over 250 μg/L (reference interval: 150 μg/L). NCC values below 50 μg/L point to the possibility of systemic copper depletion in individuals receiving protracted therapy [12],[13].

As technology has improved, diagnostic processes have become more advanced, precise, and reliable. This is due to many aspects, such as the discovery of new techniques, the analysis of new markers, or improvements in materials for device fabrication.

In recent years, the discovery of LIG has led to the development of low-cost and flexible electrodes that can be easily integrated and/or functionalized to monitor many biomarkers. LIG electrodes can also be used to detect low concentrations of heavy metals [14].

The main advantage of the LIG method is its versatility. This technique was first applied to polyimide substrates, but it is possible to synthesize graphitic structures in different kinds of substrates, from other polymers to carbon-based materials such as cellulose paper [15]. This technique also allows to easily explore different electrode architectures, as it is simply necessary to make the design on photoshop and send it to the laser program. Upon optimizing the laser conditions to the type of substrate it is possible to obtain electrodes with very good conductive properties and maintain the advantages that the graphene usually displays [16].

The use of paper is growing in the electronics sector, with cellulose-based materials being utilized in sensors, batteries, foldable printed circuit boards, capacitors, and transistors among others [17]. LIG on paper [18] made it possible to engrave highly conductive graphitic material in predetermined patterns on this substrate in a single process, expanding the substrate's potential uses as, for instance, a platform for sensing devices.

1.2 Aim and Dissertation Plan

The goal of this thesis is to create planar electrochemical cells using the LIG process on environmentally friendly substrates, specifically a DLHC substrate supplied by Alma-Science and a cellulose-based Whatman 1 paper. These electrodes will subsequently be used in a biological detection system with an integrated microfluidics channel to diagnose and monitor WD patients throughout their many treatment phases.

The project has been divided in two phases. The first took place at CENIMAT in Lisbon, Portugal, where the fabrication method was optimized, along with a study of the characteristics of graphene and the electrode architecture. The electrochemical cells were tested for heavy metal detection at low concentrations and integrated in a detection system along with a microfluidics channel designed for copper detection at low concentrations during the second stage, which took place at the ICN2 in Barcelona, Spain.

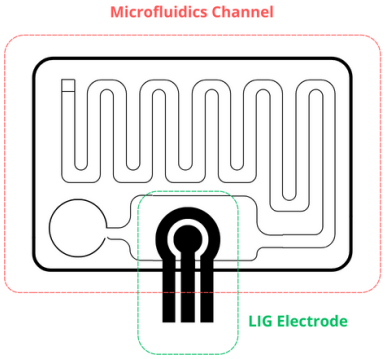

Figure 1.1: Schematic of the Biological Detection System for Heavy Metal Detection.

A microfluidic channel was designed to perform copper measurements through sweat or urine samples. This is a way to prevent contamination, since it is idealized that the biofluid would be contained in the channel so there would be no contaminations, the device would be easier to handle, and at the same time a way to try to optimize the sensing capabilities of the electrode.

The LIG and microfluidic channel was synthesized/fabricated using a commercial CO_2 laser, enabling complete production via laser technology. This approach ensures precision and accuracy in the manufacturing process, resulting in a high quality end product. By using a single system for both the LIG and the microfluidic channel, time and resources can be saved, making production more efficient. The use of the CO_2 laser provides a versatile and reliable platform for the manufacture of these components.

The research work described in this dissertation was carried out in accordance with the norms established in the ethics code of Universidade Nova de Lisboa. The work described and the material presented in this dissertation, with the exceptions clearly indicated, constitute original work carried out by the author.

2

Theoretical Concepts

2.1 Biosensors

One of the areas of biomedical engineering that has received the greatest amount of research is biosensors. It is a very broad field with a significant impact on several societal sectors, including food, pharmaceuticals, healthcare, and environmental monitoring. The goal in the biosensors field is to create devices that combine user friendliness, low production costs, great analytical precision and little complexity [19].

Biosensors are analytical devices that convert a binding event of the analyte into the bioreceptors in a quantifiable and processable signal. These devices are categorized by their detection methodologies, where the electrochemical biosensors, the focus of this study, stand out due to their high analytical performance in terms of sensitivity, selectivity, and response time, paired with low cost, portability, and robustness. Despite all these advantages, there are several aspects that held back the emergence of additional breakthrough applications built on electrochemical biosensing [20].

2.1.1 Electrochemical biosensors

Electrochemical biosensors convert biochemical occurrences like enzyme-substrate reactions and antigen-antibody interactions to electrical signals (e.g., current, voltage, impedance, etc.). Since Clark created the first electrochemical biosensor for measuring blood glucose [21], numerous other types of biosensors have steadily been researched and made commercially available for a variety of uses. In most cases an electrode serves as a solid foundation for the immobilization of biomolecules (e.g., enzymes, antibodies, and nucleic acids) and the transportation of electrons in most electrochemical biosensors. In recent years the trend in biosensing is to commercialize smaller analytical devices for on-site analysis, in order to replace big-sized lab instruments [22].

Due to the lack of surface architectures that allow high enough sensitivity and selectivity in electrochemical biosensors, most of the breakthroughs in the last decades have come from the introduction of nanotechnology and innovative materials to create new generations of more sensitive, highly specific, reliable, and even smaller and cheaper

sensors [23]. The development of biosensors has changed due to the use of readily accessible and inexpensive carbon-based materials, such as graphene, carbon nanotubes, and other carbon nanostructures in their manufacturing due to their superior capacity to transport electrons and high surface-to-volume ratio, enhancing the analytical power of these systems. However, the fabrication of carbon-based devices into intricate patterns with a variety of desirable configurations makes the use of conventional lithographic processes challenging. The use of these materials makes the exploring of different device architectures hard due to their reduced flexibility, which raises the concern for alternative microfabrication techniques [24],[25].

2.1.1.1 Electrochemical principles

The study of electrochemistry is concerned with the understanding of electrochemical processes. At an electrode/solution contact, these reactions include the transfer of charges [26]. The electronic flow of charges across the interface between an electrode, an electron source, and an aqueous solution is portrayed by the RedOx reaction. It is important to note that this phenomenon only happens once an electrode has been inserted into the solution and is functioning as a source or destination for traveling charges. These particles move throughout the area where the electrode and solution are interfacial, creating a differential potential at this location [27].

A dynamic electrochemical reaction's general process, in which the reactant, the oxidized species, first diffuses from the bulk solution to the electrode/solution interface by a mechanism known as mass transport. The system is then subjected to a potential difference that is different from the equilibrium, causing charge transfer between the electrode surface and solution. The molecules become oxidized thanks to the moving electrons. The reduced species, which in this case are the reaction's byproduct, diffuse into the bulk solution by mass transfer. Depending on the potential that is being used, this process may go either way [27].

The ability to analyze chemical reactions, adsorption/desorption, and heterogeneous electron transfer rate is made possible by the current generated at the electrodes since these processes are connected to mass transfer, which is what causes the change in potential [27].

2.1.1.2 Cyclic Voltammetry

One of the most often used electrochemistry instruments, CV, is recognized as one of the best ways to assess the electrode kinetics. By enabling the monitoring of the thermodynamics of particular Redox couple reactions, the kinetics of heterogeneous electron-transfer processes, and other processes like adsorption/desorption, CV has, for the past decades, been widely used in the qualitative study of electrochemical reactions.

In CV, a potential is applied to an electrode submerged in an electrolyte solution, and the system then monitors the current in funtion of the potential applied. In CV,

an aqueous solution containing the target component is subjected to a linear sweeping voltage. A CV consists of linearly scanning the potential applied to the Working Electrode (WE) from a preselected initial potential E1 to a desired limit potential E2, at which point the direction of the scan is reversed until it reaches E1 again, concluding the cycle.

As displayed in 2.1, the current resulting from the applied potential is measured using a potentiostat and is plotted in a current (I) vs. applied potential/voltage (E) graphic designated as cyclic voltammogram. The x-axis represents the potential energy (in volts) imposed on the system throughout the cycles. At the same time, the y-axis is a scale for the electrode response, representing the resulting current (in amperes) [28]. CV can be performed against a multitude of electroactive species, but one of the standard redox probes used in electrochemical studies is the ferri-ferrocyanide redox couple characterized by its well-defined oxidation and reduction current peaks shown in 2.1.

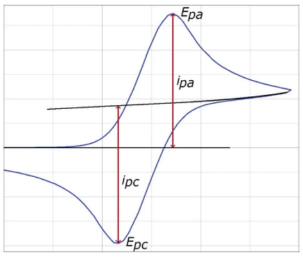

Figure 2.1: Common CV data demonstration, IUPAC format. Adapted from [29]

2.1.1.3 Square Wave Anodic Stripping Voltammetry

SWASV is frequently used to determine HM concentrations in water or biofluids. It has found various applications in environmental studies of polluted bodies of water [30]. In this project, we used this electrochemical technique for detecting copper (Cu) in acetate buffer. It is a form of linear potential sweep voltammetry that uses a combined square wave and staircase potential applied to a stationary electrode [31]. For the detection of HM using SWASV, there are three main stages: the deposition phase, the equilibrium phase, and the stripping phase. Initially, the WE applies a constant potential to the analyte sample for a specified period of time during the deposition phase. Subsequently, the HM analyte is reduced and deposited onto the WE. After the deposition time ends, stage two begins. In this stage, no current is applied for a set amount of time called equilibration time. Once this time has passed, Stripping commences. The current at the WE is measured by pulsing the potential between it and the reference electrode forward and backward at a constant frequency [30]. The current is sampled twice - at the end of the forward potential pulse and again at the end of the reverse potential pulse. This sampling technique minimizes the contribution of capacitive current to the current signal. Although both the forward and reverse current waveforms have diagnostic worth, the potentiostat software typically generates a differential curve by subtracting the reverse current waveform from the forward current waveform. This differential curve is then plotted against the applied

potential [31],[32]. The SWASV data analysis involves identifying peaks in the differential curve, which correspond to the analytes that have been reduced and subsequently oxidized during the experiment [31]. The intensity of each peak is proportional to its corresponding analyte concentration [31]. Using these principles, it is possible to determine copper concentrations in urine, sweat or other body fluids.

2.2 Graphene

Graphene is a carbon-based material comprising a single sheet of densely packed carbon atoms in a hexagonal pattern due to its benzene-ring structure. In recent years, the closely packed honeycomb carbon lattice of graphene has gained considerable attention in the electrochemistry field due to its intrinsic properties and advantages [33].

Graphene is currently the strongest and thinnest substance known to man. Since its production necessitates exposure to extremely high temperatures and thermal fluctuation, graphene is the first 2D atomic crystal structure to be identified that seems to defy the normal crystallization process. Graphene may be found or reshaped as fullerenes (0D dimensional), rolled into 1D nanotubes, or if stacked can form graphite (3D structure) [34],[35]. Graphene's existence was generally known, but it wasn't until Novoselov and colleagues [35] used micromechanical exfoliation in 2004, that they were able to isolate it [36]. Other methods of production have subsequently been created, however these conventional approaches, such as Chemical Vapor Deposition (CVD) or chemical exfoliation, either need for high-temperature processing or multi-step chemical synthesis, which limits the economic viability of this material [37].

In 2014, it was discovered that 3D porous graphene in the form of LIG can be generated through direct writing on commercial polyimide films using a CO_2 infrared laser under ambient conditions [38],[39]. Systems based on LIG have come to bridge the gap between these carbon based-materials that present many useful properties, specifically graphene, and the drawbacks that their fabrication techniques present, thus making the laser processing approach more and more popular in industry [40].

The process of fabricating LIG includes irradiating a polymer substrate with a laser beam, resulting in the formation of a graphene-like structure. During the process, the laser beam dissolves the polymer's carbon-oxygen and carbon-nitrogen bonds, releasing gases like carbon monoxide and methane. The carbon atoms then combine to form the graphene-like structure on the substrate's surface. The LIG structure produced is a porous material with a high surface area, thereby making it an optimal candidate for electronic sensors and energy storage devices [41].

Compared to traditional graphene fabrication techniques, LIG offers several advantages. According to Huang et al. LIG technology is environmentally friendly, and both its compositions and morphologies are adjustable [42]. Additionally, it exhibits exceptional electric and thermal conductivity, high porosity, considerable flexibility, and mechanical

robustness [41]. LIG is also printable and patternable, making it an ideal material for producing miniature graphene devices for various fields such as battery technology, catalysis, and sensing applications [42].

2.2.1 Laser specifications and parameters

On the laser engraver software, it is possible to control the power as a function of the percentage of the maximum power (50 Watts (W)), control the speed of the laser nozzle and the number of Points Per Inch (PPI). These parameters are used to optimize the graphitization of the different substrates. Different combinations of Power (P) and Speed (S) produce different results: for example, if the power is too low and the speed is high, it has no effect on the substrate, and if the power is high and the speed low it may cause ablation, so finding the right parameters for the laser is a fine-tuning process named as processing window. After the previously referred laser parameters are set on the laser software, the laser operates with a certain frequency and pulse duration calculated from the values inserted. The pulse repetition frequency is calculated as a function of scan speed and PPI through equation 2.1:

$$Pulse\ Repetition\ Frequency\ (PRF) = \%speed * max\ speed(50 inches\ s^{-1}) * PPI \quad (2.1)$$

After, from the speed value and the pulse frequency calculated, the system adjusts the pulse duration or Pulse-width (PW) to match the power percentage chosen in the engraver's software by using equation 2.2:

$$PW(s) = (\frac{1}{PRF}) * \%power \quad (2.2)$$

The PW controls long the laser must be active at 50 J to achieve the desired power (J/s). Because of this, it is important to have in consideration that each laser pulse has a charge and cool-down time, each of 120 µs, which makes each turn-on turn-off cycle of 240 µs plus the PW that is chosen.

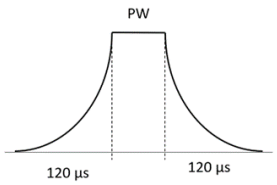

Figure 2.2: Schematization of a full laser pulse cycle.

The distance between the laser nozzle and the paper substrate also has an important role in the quality of the graphitization. It was previously verified at CENIMAT that the best configuration is to have the height of the substrate plane on Z= -0.1 in [43]. This configuration allows for the laser beams to impact the paper in a convergent beam. In that way the electrode delimitations are more clearly defined. Also, having the Z at -0.1

in increases the spot size of the beam from 127 μm^2 obtained at Z= -0.07 in (default value for the smallest spot size). Since the spot size has a bigger area there is some overlay of the irradiated area between two consecutive pulses which guarantees a better continuity of the graphene conversion throughout the paper.

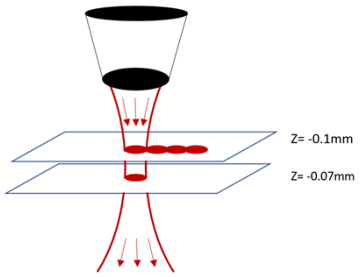

Figure 2.3: Schematization of the laser nozzle and beam.

2.3 Cellulose substrate

The choice of the substrate is also a crucial step to the fabrication of the electrodes, since its properties can influence the analytical qualities of these devices. By choosing to use carbon-based substrates such as paper, due to it being environmentally sustainable, there is drawbacks that must be accounted for. Although cellulose substrates are widely available, inexpensive, flexible, and sold in a variety of porosities, thicknesses, and with various additives [23], they cannot withstand the power of laser cutters. These cutters are used to induce graphitization onto cellulose molecules through irradiation, which causes thermal degradation and ablation to the paper. Fire-retardant chemical treatments, such as sodium tetraborate, have been used to lessen the heat damage and ablation when these substrates are subjected to laser irradiation [18]. Paper substrate also has a second disadvantage: due to its porosity and chemical composition it is usually a hydrophilic material which is not ideal for the use in an electrochemical biosensor. One common solution to this issue is impermeabilization, which can be achieved by wax-printing a coat of wax and melting it to fill the paper pores, creating impermeability [44]. Another way, that we explored in this work with the DLHC substrate, is to use compressed cellulose fibers as means of impermeabilization.

3

State of the Art

3.1 Graphitization techniques

There are many types of electrodes produced from various materials, including platinum, gold, gold nanoparticles, carbon, carbon nanotubes, and graphene [44]. Because of its physical-chemical features, graphene has attracted a lot of attention [45]. There has been a rush to optimize graphene synthesis, which has resulted in a variety of production methods [45].

3.1.1 Laser-Induced Graphene

Laser-induced graphene (LIG) is a three-dimensional porous material obtained by irradiating a laser beam on to polymer or carbon-based materials by a CO_2 laser [38]. This graphitization technique was first developed on polyimide substrates. Tour's group reported the production of porous graphene films from commercial polyimide sheets using a CO_2 laser back in 2014 [39]. The LIG studied by the group presented very good characteristics, such as a high surface area (approximately 340 m2 g^{-1}), high thermal stability (>900ºC) and excellent conductivity (5-25 S cm^{-1}). They also characterized the porous graphene films on SEM and Raman spectroscopy. The team also fabricated electrodes with this technique [46]. The results for LIG in polyimide were positive which propelled the application of this technique to different substrates such as other polymers and carbon-based materials. Cao et al. 2020 used a CO_2 laser to efficiently convert the synthesized poly (Ph-ddm) into LIG in order to find a possible LIG precursor with outstanding durability under harsh conditions. The poly (Ph-ddm)-based LIG demonstrated a low sheet-resistance of 35 Ohm sq^{-1} as well as a high specific surface area of 883 m2 g^{-1}. And due to the superior features of poly (Ph-ddm), the LIG patterns demonstrated exceptional resistance to strong acid/base solutions as well as great adherence on the substrate, ensuring their durable application under harsh conditions [40]. At CENIMAT this approach is used for creating graphene electrodes on carbon-based substrates, more precisely paper. A systematic study was conducted and the results were positive in terms

of electrical, surface chemistry characterization, and electrochemical characterization. Pinheiro et al. obtained LIG electrodes with sheet-resistance as low as 56 Ω/sq, Raman spectra showing the characteristic D, G, and 2D peaks of graphene, with I_D/I_G and I_{2D}/I_G ratios of 1.281 ± 0.173 and 0.616 ± 0.095, respectively, and Heterogeneous Electron-transfer Rate Determination (k^0) values as high as 7.15 x 10^{-4} cm s^{-1}. This verifies the capabilities of paper-based LIG for the efficient development of disposable electrochemical sensors.[44].

3.2 Heavy Metal Electrochemical Biosensors

The current trend for HM detection in water moved away from the conventional mercury electrodes, after the concerns raised for its toxicity, followed by its prohibition after the European Directive 2008/105/ECThe [47]. Depending on whether the goal is HM pollution detection in industrial waste or drinking water analysis, detection limits in the μM or nM range must be reached, respectively. The detection of trace metals requires sensitive methods. It is within this framework that Pujol et al. presented contributions of the French scientific academic community in the field of electrochemical sensors [48]. The combination of amperometric transduction with the specificity induced by the modifier makes it possible to propose reagent-less sensors exhibiting high sensitivity and good selectivity [48]. They also discuss the large range of available strategies for surface modification. These strategies are stripping voltammetry, solid mercury-free electrodes, and nano-structured surfaces. They also discuss the material modifications that are possible in these kinds of electrodes such as using ecofriendly alternative electrode materials as graphite, Boron doped diamond or diamond like carbon [48]. A new generation of analytical devices called micro total analysis system (mTAS) is being developed for the online monitoring of real samples. These devices integrate not only the sensing element but also some complementary actuators (pumps, valves, microfluidic channels) to obtain an all-integrated automatic monitoring system which includes a calibration procedure [48].

3.2.1 Copper detection devices

Lin et al. investigated the detection of copper ions using iminodiacetatic acid (IDA) modified conducting copolymer electrodes [49]. This is a modified electrode capable of specifically selecting copper ions in multi-HM solutions. Due to the presence of a long spacer between the matrix and the iminodiacetate groups, the IDA-modified copolymer electrode has better functional group flexibility and is therefore expected to have improved metal ion binding properties. This electrode is capable of determining metal ions in the range of 0.1-10 µM, 6.35 - 635 ppb. Although this electrochemical cell exhibits good performance and selectivity for copper measurements, it is made of a modified copolymer, which is not environmentally friendly and requires a long chemical process for polymerization and modification of the copolymer film [49].

Yang et al. [30] developed an autonomous sensor boat capable of detecting HM in water samples to measure their risk to the environment. Techniques such as Atomic Absorption Spectrometry and Inductively Coupled Plasma Spectrometry, etc. are the gold standard techniques for HM detection but require the use of big laboratory equipments that are not practical for in-site measurements. However, to create a portable system that can be used on the field, they took advantage of the portability and rapid detection capabilities of electrochemical testing by using SWASV. The sensing boat consists of a fluid Heavy Metal sensing system (FSS), which is the main part of the device, and an electronic control system that determines when to start a peristaltic pump and mixer system. The mixer is important because the authors need to mix the sample with electrolytes. The main component of the FSS is the electrode where the redox reaction takes place [30]. This screen-printed carbon electrode was able to measure copper concentrations with a Lower Limit of Detection (LOD) of 0.3 ppb or 0.3 µg/L when diluted with deionized water and 6 µg/L when mixed with other HM in the same solution. Yang et al. were able to achieve very low LODs for copper. In this project, we are trying to explore copper detection using LIG electrodes, which have a simpler and faster fabrication process and are more environmentally friendly than screen-printed electrodes, and without the need to mix electrolytes with the sample of interest.

In another work, Yang et al. propose an all-printed wearable system for electrochemical copper detection and its concentration normalization with sweat rate [50]. This wearable device consists of three main parts, an inkjet-printed microfluidic channel, a screen-printed carbon electrode, and a flexible potentiostat that transmits the collected data to a smartphone. Yang et al. also implemented an iontophoresis module in the device. This module is capable of stimulating the sweat glands to collect sweat samples on demand. According to the authors, this device has many advantages over other HM detection devices because it is easy to fabricate, low cost, and the device is lightweight and compact. Copper measurements were performed using the SWASV electrochemical assay and by diluting a copper standard solution in artificial sweat. With this device, they were able to obtain a LOD of 396 ppb with a sensitivity of 2.3 nA/ppb [50]. This device also allows the microfluidics to be reused by placing a sponge at the outlet to clear the channel of liquid. During the project of this dissertation, we also aim to achieve a small and compact device that combines microfluidics with an electrochemical cell [50]. Taking this device as inspiration we aim to acheive a sensor capable of reaching a LOD low enough that would permit the diagnosis of WD. Our device is idealized to have an all-laser fabrication, from the eletrochemical cell to the microfluidics channel.

4

Materials and Methods

4.1 Materials

To produce the chemical solutions and fabricate the biosensing device a variety of chemicals and materials were used. Ultrapure Milli-Q water was used for the preparation of all chemical solutions. The Sodium tetraborate decahydrate solution ($Na_2B_4O_7.10H_2O$) was formulated using the Sigma Aldrich reagent. To create the AB with a pH of 4.5, a combination of Acetic Acid >99% (CH_3COOH) and Sodium Acetate ($C_2H_3NaO_2$), both obtained from Sigma Aldrich, was used. Standard HM solution Cu 1000 parts per million (ppm), AAS grade, was purchased from Sigma Aldrich.

For the LIG production, a Double-layered hydrophobic cellulose DLHC paper was synthetised by AlmaScience, and Whatman paper grade 1 was purchased from Whatman International Ltd., Florham Park, NJ, USA, to serve as the substrate for the LIG electrodes. The substrates went through different LIG production protocols. The Whatman 1 paper must be impermeabilized by wax coating while the DLHC substrate does not need to undergo this process. The Whatman 1 paper underwent treatment with four layers of wax printing using a Xerox ColorQube printer. A6 plastic lamination pouches from Staples were used to laminate the electrodes, providing both structural stability and encapsulation. To coat the electrode contacts, we utilized AG-510 silver ink, provided by Conductive Compounds, Inc., Hudson, NH, which is a silver conductive ink. For the Reference Electrode (RE), we used AGCL-675 which is an Ag/AgCl ink, also from Conductive Compounds, Inc., Hudson, NH. To create a microfluidic channel, we layered two glossy Polyethylene terephthalate (PET) sheets and adhered them with a double layer of A4-sized Bi-Adhesive sheets.

4.2 Experimental Fabrication Equipment

4.2.1 Commercial CO_2 laser

Every aspect of the fabrication of the LIG electrodes was completed at CENIMAT, NOVA University of Lisbon. The primary equipment employed for this process was a

commercial CO_2 laser, in particular, a VLS 3.50 desktop laser by Universal Laser Systems. The particularities of the laser have already been explained upon in the 2.2.1 section. The initial step needed to operate the laser involves uploading an Adobe Illustrator document to the laser software that contains the pattern for the electrode to engrave or the outline to be cut. The input file requires a specific colour in the Red Green Blue (RGB) format. This is crucial for the laser software to recognise the shapes and allow the user to encode the desired laser Power, Speed and Pulses per Inch PPI. These settings are essential to cut through a material or to engrave the electrodes. The Power setting can vary between 0.1% to 100%, with the percentage chosen representing a fraction of the maximum laser power which is 50W (100%). The Speed setting follows the same principle whereby the laser nozzle's maximum speed is 127 cm s^{-1} in Rast Mode and 25.4 cm s^{-1} in Vect Mode. The Rast and Vect modes differ in that the former applies the laser beam via a series of linear pulses layer by layer, while the latter applies the pulses along the vectorial lines of the design. The PPI setting determines the number of laser pulses emitted per inch and ranges from 1 to 1000 PPI. This setting significantly affects the results because a higher PPI may stress the substrate, while a lower PPI may result in interrupted engraving due to more or less overlapping [51]. Finally, it is necessary to establish the distance between the laser support rake and the nozzle, as previously reported in the 2.2.1 section. This setting, known as the Z coordinate, affects the laser's effectiveness because of the plano-convex focal lens, which creates an ideal spot size of incidence depending on its distance from the substrate.

4.2.2 Oxygen Plasma Cleaner

During assembly of the microfluidic channel, it's crucial to clean and activate the PET surface to ensure steady analyte flow through the narrow channel. This is possible through the use of oxygen plasma, which increases the hydrophilicity of this component. Oxygen plasma cleaners use oxygen plasmas to eliminate organic contaminants from different surfaces and materials [52]. To generate oxygen plasmas, an electric field is applied to a gas mixture with oxygen, which ionizes the gas molecules and forms a plasma including electrons, ions, radicals, and photons [53]. The Plasma cleaners work by exposing the surface to be cleaned to plasma. The plasma reacts with the organic contaminants and breaks them down into volatile products, like carbon dioxide and water. These volatile products are then cleared out of the chamber, resulting in a clean and activated surface [54].

4.3 Characterization Equipment

4.3.1 Hall Effect Measuring System

In optimizing laser parameters for LIG engraving on the Whatman 1 cellulose substrate, the HL5500PC Hall Effect Measuring System played a crucial role. This system allowed

for the calculation of the Sheet-Resistance of samples with varying laser parameters, a key indicator of the best LIG electrodes as it measures the material's resistance to electrical current flow [55]. To determine the Sheet-Resistance, four silver paint dots are painted on the edges of a 5mm x 5mm square. These dots serve as the contacts between the probes of the Hall Effect System and the sample. Once the four probes are in place, a current is applied between two probes at a time. Therefore, it is crucial for the shape to be as symmetrical and homogeneous as possible. The device then provides resistance values between each pair of probes and calculates an average for the sample [56]. The one used at CENIMAT can measure resistivities in the range of MOhm square^{-1}.

4.3.2 Raman Spectrometer

Raman spectroscopy was used to analyze the molecular structure and properties of the LIG samples by studying the interaction between light and the material [57]. This technique employs a beam of monochromatic light (laser) that irradiates the sample, causing scattered photons to disperse in different directions. Most of the dispersed photons retain the same energy and wavelength as the incident photons, a phenomenon known as Rayleigh scattering. However, a few of the scattered photons have distinct energies and wavelengths, which is referred to as Raman scattering [57].

The spectrometer measures the energy difference between incident and scattered photons, which equals the energy of a vibrational mode. These vibrational modes indicate the stretching and bending movements of chemical bonds, and they have unique frequencies that are dependent on the mass and stiffness of the atoms involved. The resulting Raman scattering spectrum shows the intensity as a function of frequency or wavelength and offers details about the molecules identity, quantity, orientation, and environment in the sample [58].

With this technique it is possible to verify if the sample has many defects and the main molecular composition, indicating, in this case the quality of the LIG after the laser engraving.

4.3.3 Scanning Electron Microscope

A scanning electron microscope SEM was employed to examine the cellulose fibers from the substrate after LIG engraving. This method is frequently employed to study bio and nanomaterials at a microscopic level. Its primary applications include investigating substrate morphology, composition, and defects [59]. SEM operates on a similar physical principle as traditional microscopy, with the exception that a high-energy electron beam is utilized rather than a light beam. The electron beam interacts with the atoms of the object of interest, resulting in the ejection of secondary electrons from the sample. These electrons are then captured by a detector, which formulates an image with exceptional depth and spatial resolution [60].

4.3.4 Potentiostat

The PalmSens4 Potentiostat was used through out the hole project to perform all the electrochemical characterization and tests. The PalmSens software has the ability to choose many different electrochemical tests such as CV and SWASV which were used to characterize and analyze the electrode capabilities and to detect HM, respectively. Potentiostats are made up by a set of electrodes, the WE, Counter Electrode (CE) and RE, and this device is no exception. The potentiostat controls very precisely the potential difference between the WE and the RE, by applying a current to the solution. The electrode on which the relevant electrochemical reaction is taking place is the WE. This location controls the potential, and the resultant current is monitored [61]. The CE ensures that the current entering the solution through the WE also exits the solution, thereby closing the circuit in the electrochemical cell. It is also important that the CE area is bigger than the WE area to ensure the flow of electrons is not hampered [61, 62]. The RE, which serves as a reference in the electrochemical cell, is a stable electrode with a known potential. The potential of this electrode should remain constant while no current is being supplied [61],[62].

4.4 Experimental Procedure

4.4.1 Pretreatment of the cellulose substrate

To induce graphitization in paper substrate, they must first be treated with Sodium Tetraborate Decahydrate Solution (0.1 M) to withstand the heat generated by the laser beam during engraving and to make the substrate impermeable to areas not directly affected by the laser. Paper sheets were cut into A6 size (105 x 148 mm). After cutting all the sheets, they were soaked in a container of 0.1M Sodium Tetraborate Decahydrate solution for 10 minutes per side. Occasionally, the sheets must be divided into multiple batches for thorough soaking. Once complete, the treated material should be dried in an oven at around 50°Celsius (C) with silica to remove any remaining moisture. When this step is complete, the paper will be more resistant to laser thermal radiation, resulting in less ablation of the cellulose fibers due to the Sodium Tetraborate Decahydrate solution acting as a fire retardant.

Contrary to the DLHC substrate, the Whatman 1 paper substrate requires four layers of wax printed onto it using a Xerox wax printer in order to be wax-coated. After each layer, the paper is placed on a hot plate at 100ºC to allow the wax to diffuse evenly throughout the cellulose fibers, ensuring a uniform coating throughout the paper thickness. As previously mentioned, this step is critical in creating a functional sensor as it makes the substrate impermeable, allowing for the placement of analyte solutions for testing and measurement.

4.4.2 LIG Electrochemical Sensor Production

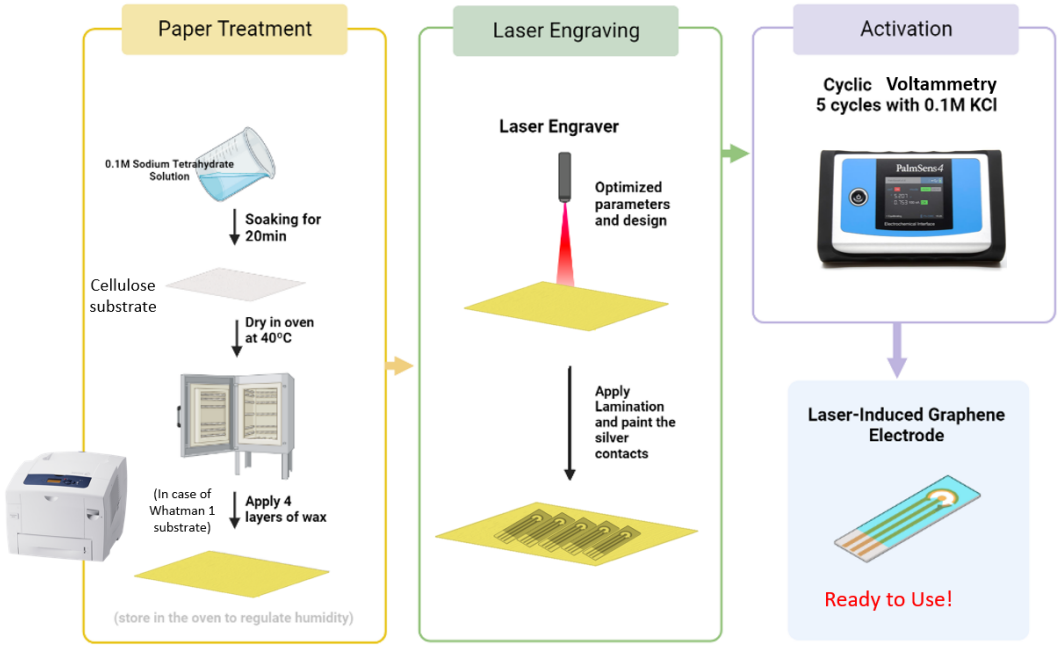

Figure 4.1: Electrochemical sensor production protocol.

To produce LIG, the paper substrate was securely attached to a glass slide using standard tape to maintain a flat and immobile surface during laser exposure. This step is essential to ensure uniform distance between all areas of the paper substrate and the laser nozzle. Next, the Z coordinate value was set to -0.1 in. To ensure consistent results, we stored the treated paper substrates in a 40 ºC oven to remove humidity before laser engraving. The laser chamber was connected to a hose that continuously supplied nitrogen.

After considering all of these steps, the design to be engraved is uploaded to the laser software. It is imperative to select Rast Mode and input the desired laser parameters (P, S, and PPI) as these factors significantly affect the outcome of the LIG. Then, the paper substrate is aligned and placed inside the laser chamber. The nitrogen hose is then opened, the exhaust is turned on, and Laser engraving can proceed.

The LIG optimization process is pre-defined. First, a matrix of 8x8 LIG samples consisting of 2x2mm squares with two variables, laser power on the X-axis and laser speed on the Y-axis, is created. Each variable ranges from 1 to 8%. Then, after visually analyzing all the samples, a selection is made for further characterization. This initial selection involves eliminating the cases where paper ablation occurred or where no visible LIG effect was present. Typically, the main criterion for choosing the optimal LIG conditions is achieving a low sheet-resistance result. After the best laser conditions are determined the LIG electrodes are produced using taking them into account. Before using the freshly made electrodes, they need to be activated through a CV process. The process involves running the PalmSens4 at -2 to 2 V with an Estep of 0.01 V and a scan rate of 0.15 V s^{-1}

for 5 scans using a solution of KCl 0.1 M. This procedure makes the graphene electrodes more hydrophilic and ensures they are ready to use.

4.4.3 Microfluidic Channel Fabrication

The fabrication of microfluidic channels involves designing them in AutoCad or Adobe Illustrator and setting the laser to Vect Mode. This approach allows the laser to follow the design continuously. The assembly process consists of two parts. The first is to cut the Bi-adhesive layer into the channel's shape, which will then be attached to the laminated electrode layer to define the channel for the solution to flow. The following component consists of a PET layer equipped with an inlet and outlet for adding the analyte. This layer undergoes an oxygen plasma cleaning treatment to increase its hydrophilicity, allowing the solution to flow by reducing surface tension. Finally, the layer is precisely positioned on top of the Bi-adhesive layer to closing the channel.

This step also requires optimization of the channel's shape for the assembly process. A variety of designs were tested to attain the steadiest flow and homogeneous filling of the electrode chamber. Additionally, various cleaning times were employed with the oxygen plasma cleaner to increase or decrease hydrophilization of the top PET layer that closes the microfluidic channel. These efforts aimed to achieve an optimal and consistent flow speed, which determines the time for the solution to reach the end of the channel for analysis.

4.4.4 Acetate Buffer Preparation and Cu dissolutions

To test the sensor/device for detecting HM in different concentration levels in bodily fluids, a 0.1 M AB solution with a pH of 4.5 was used to dilute the Copper. To produce this solution, a container was prepared with a specific amount of MilliQ water, and the appropriate amounts of Sodium Acetate (136.09 g mol^{-1}) and Acetic Acid (60.05 g mol^{-1}) were added. The pH of the solution is adjusted by adding hydrochloric acid or sodium hydroxide, followed by additional MilliQ water until the desired volume is reached. After the AB is prepared, dissulutions of 1000, 500, 200, 100, 50, 10, and 1 ppb diluting the Cu Standard HM solution in AB were made.

5

Results and Discussion

The current chapter reports all developments achieved from the experimental stages of this work. Laser parameter optimization results are described and Copper detection tests are displayed and all the findings are analyzed and discussed, leading to the final remarks presented in the concluding chapter.

5.1 Laser Parameter Optimization for LIG electrodes fabrication

To achieve the best optimized LIG electrode, numerous characterization tests were conducted. In the initial phase of the project, discussions with the supervisors from CENIMAT and ICN2 revealed an idea to utilize a recently manufactured paper substrate by AlmaScience, DLHC. The aim of using this substrate was to expedite the production process by omitting wax from the paper treatment protocol, while simultaneously preserving the impermeability it provided. The substrate consists of two distinct layers: a compressed cellulose fiber layer that is impermeable and a regular paper sheet layer which provides structural support for the entire substrate. Both substrates, DLHC and Whatman 1, were subjected to characterization methods with these considerations in mind.

We initiated the characterization process by using a Power vs. Speed matrix to exclude laser parameters causing substrate ablation or insufficient graphitization. This allowed us to concentrate on fewer parameter combinations for subsequent tests. We conducted sheet-resistance tests on selected LIG samples. Chemical and morphological tests were performed to provide a better understanding of the molecular structure of LIG and the physical changes in the paper substrate following laser irradiation.

Finally, we conducted electrochemical characterization tests on the selected parameters using a potentiostat. We performed CV against an iron redox probe solution, which allowed us to determine theElectrochemically Active Surface Area (ECSA) and the k^0. After conducting these tests, we were able to identify the optimal laser parameters for LIG fabrication.

5.1.1 Power vs. Speed Matrix

In order to create a functional LIG sensor on a paper substrate, it is essential to conduct an initial test to assess the impact of the laser on the substrate. The most effective approach to testing various P and S percentage combinations of the laser is to generate a 2 x 2 mm matrix on the paper substrate with variations ranging from 1-8% in 1% increments, equating to 0.50-4 W for power and 1.27-10.16 cm s^{-1}.

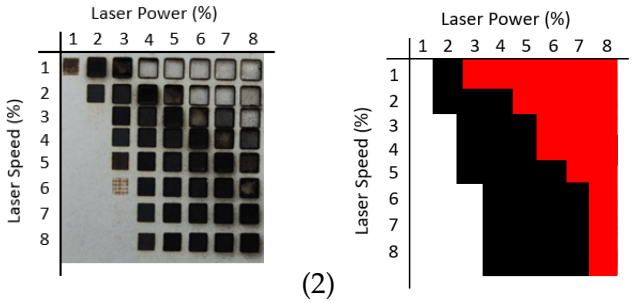

(1) (2)

Figure 5.1: Laser Power vs. Speed matrix for DLHC paper substrate at z = -0.10in.

Referring to Figure 5.1, the Power vs. Speed matrix for the DLHC substrate displays three distinct areas that are key on the laser beam's interaction with the substrate. It is evident that the primary LIG synthesis area is the diagonal section running from the top left to the bottom right. This implies that to apply the same amount of energy in less time, power must be increased in unison with speed. When increasing the Power over the Speed, it was observed that paper ablation occurs more frequently.

Upon examination of a heat map of these settings, three distinct areas become easily identifiable. Figure 5.1(2) reveals an area on the lower left where little or no graphitization occurred. This is due to insufficient energy absorbed by the substrate to break the bonds of the cellulose fibers and convert them into carbon rings, the typical graphene like structures. This is frequently observed in combinations of high speed and low power which are more represented in the white part of the map. The opposing results are seen in the red region of the heat map, where the substrate experiences ablation owing to higher power percentages combined with low laser speeds. This results in excessive energy absorption by the substrate and causes the destruction of all chemical bonds within the cellulose fibers, leading to surface perforation and paper burning. Therefore, it can be deduced that the LIG synthesis must have well-considered and balanced settings. Sufficient energy must be applied to break cellulose bonds and convert them into carbon rings, while ensuring that all bonds are not broken, leading to paper burning. Figure 5.1(1) shows these results on the main diagonal, which correspond to the black area of the heat map in Figure 5.1(2), indicating equilibrium and successful LIG formation.

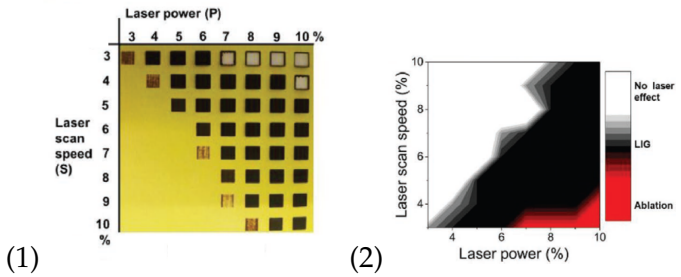

Figure 5.2: Laser Power vs. Speed matrix for Whatman 1 paper substrate at z = -0.10in. Adapted from Pinheiro et al.[44]

To choose laser parameters for Whatman 1 paper substrate, we based our work on Pinheiro et al.'s research at CENIMAT and conducted a variety of laser parameters for further characterization. From analyzing Figure 5.2, adapted from Pinheiro et al., we can distinguish three main areas of laser interaction [44]. This suggests that the matrix from Figure 5.1(a) created with a different substrate closely aligns with literature produced with similar substrate material. The optimal laser and power percentages obtained from this literature were identified as coordinates P7S8 (Power 7%, Speed 8%).

5.1.2 Sheet-Resistance Mesurements

After analyzing the Matrix comparing Power and Speed, we conducted measurements of sheet-resistance to perform electrical characterization. We selected laser percentage parameters based on this experiment's objectives. We tested two different laser setup heights: the first with one glass panel making z=-0.14 inches (H1) supporting the paper substrate and the second at the same laser bed height but with two glass slides (H2) on top of each other, making z=-0.18 inches, supporting the substrate closer to the laser nozzle and creating more overlapping laser incidence. Furthermore, we experimented with three distinct laser parameters: We conducted these experiments to determine the most effective laser settings for our purposes. P6S6, P7S7, and P7S8. The table 5.1 displays the sheet resistance data for each sample and the mean resistive value for each laser parameter, accompanied by their respective standard deviation values. Upon examining the mean values, there is evidence of an alteration in resistivity due to a change in height. Notably, this change was more pronounced when observing P6S6 laser parameters. At z=-0.14 inches, the average resistivity was found to be 36.17 ± 1.06 Ω/sq. Conversely, at a height z=-0.18 inches, this average increased to 54.85 ± 5.89 Ω/sq. This represents a significant 19.8% increase.

This pattern was less prominent for the remaining laser parameters, despite the double glass slide displaying lower performance when contrasted to the standard lasing process. All-in-all, the highest sheet-resistance for the z=-0.18 inches was 63.15 ± 5.12 Ω/sq for P7S8 and the least resistive values were observed for the P6S6 parameter at 54.85 ± 5.89 Ω/sq. For the z=-0.14 inches, the top sheet-resistance value obtained was 36.17 ± 1.06 Ω/sq at P6S6, while the worst result was 64.51 ± 3.38 Ω/sq. It was observed that the height

difference had a more significant impact at lower laser power, and this difference started to diminish as the power and speed were increased. Since the lower sheet-resistance samples were obtained at P6S6, we infer that the equilibrium of these parameters allows for deeper interaction of the laser with the substrate, resulting in a higher level of graphitization in a more uniform manner. With higher power, there is an increased risk of substrate perforation. To prevent excessive energy absorption by the substrate, the speed must also increase. Additionally, even when perforation does not occur, higher power can destroy cellulose fibers, resulting in lower quality graphitization and more resistive samples. Therefore, we discarded the possibility of fabricating sensors with double glass height (z=-0.18 inches) and returned to the standard protocol.

Table 5.1: Table of Sheet-resistance measurements for DLHC substrate with two different heights. (H1) z=-0.14 inches and (H2) for z=-0.18 inches.

Sheet-resistance (Ω/sq)	**P6S6(H1)**	**P6S6(H2)**	**P7S7(H1)**	**P7S7(H2)**	**P7S8(H1)**	**P7S8(H2)**
Average resistivity	**36.17**	**54.85**	**42.57**	**49.51**	**64.51**	**63.15**
Standard deviation	**1.06**	**5.89**	**7.13**	**6.25**	**3.38**	**5.12**

Pinheiro et al. reported that one of the optimal laser parameters for height z=-0.1 inches are Power 7 and Speed 8. Subsequent studies suggest that a double laser irradiation method consisting of a first pass with P7S8, followed by a second pass with P7S10, may yield superior LIG electrodes. To test both variations, sheet-resistance measurements were taken from six different samples. The results, including the average resistivity, standard deviation, and relative standard deviation, can be found in Table 5.2.

Although both variations in the laser parameters yielded positive sheet-resistance results, the double-pass laser (P7S8+P7S10) produced superior results compared to the single-pass (P7S8). The average resistivity of P7S8 was found to be 18.62 ± 3.29 Ω sq^{-1}, with a relative standard deviation of 17.66%. It was observed that low resistivity LIG electrodes are more sensitive than high resistivity ones. When compared to the resistivity of P7S8+P7S10, which was 9.68 ± 1.16 Ω sq^{-1} with a 12.02% relative standard deviation signifying a 51.98% reduction in resistivity. From the electrical characterization results the double pass irradiation method seem to be more promising, but since they both present very low sheet-resistance values this variable might not have a big impact on the final sensor.

Table 5.2: Table of Sheet-resistance measurements for Whatman 1 paper substrate.

Sheet-resistance(Ω sq^{-1})	**P7S8**	**P7S8+P7S10**
Average resistivity	**18.62**	**9.68**
Standard deviation	**3.29**	**1.16**
Relative Str. deviation (%)	**17.66**	**12.02**

5.1.3 Chemical Characterization

To conduct a chemical structure analysis and evaluate the quality of the fabricated LIG, we utilized Raman Spectroscopy. Standard Raman Spectra for LIG samples exhibit three distinct and noticeable peaks, including the D peak, typically found around 1300 cm^{-1}. This peak provides information about structural imperfections and distortions in the graphene layer, such as bent sp^2 carbon bonds. The 1600 cm^{-1} G peak arises from the first-order inelastic stretching vibrations of the sp^2 carbon bonds, revealing information on the carbon ring bond symmetry and overall molecular order in graphene [46, 63]. The 2D peak, around the 2700 cm^{-1} Raman shift, is the result of second-order zone-boundary phonon resonance. The presence of these three peaks and the fact that they are sharp peaks suggests that the formation of graphene or graphene-like material is of good quality with a low number of defects [64]. Analysis of Figure 5.3 reveals that the graphene-like material produced with the respective laser parameters was of high quality.

When analyzing a Raman spectrum, useful information can be obtained from peak intensity ratios. The key ratios to consider include the I_D/I_G ratio, which evaluates graphitization quality and defects within the graphene structure, and the I_2D/I_G ratio, which characterizes graphene layers and determines whether it is monolayered (I_2D/I_G > 2) or multilayered [63]. Upon computing the ratios for the P7S8 laser parameters in Whatman 1 paper substrate, plot 5.3(1), we have inferred an I_D/I_G ratio of 0.52, suggesting a relatively low number of defects in the carbon structures. Additionally, an I_2D/I_G ratio of 0.53 was observed, indicating the presence of multilayered graphene-like material. Meanwhile, for the P7S8+P7S10 laser parameters for Whatman 1 substrate, graph 5.3(2), the I_D/I_G ratio was slightly elevated at 0.57, suggesting a higher number of defects compared to the P7S8. Conversely, the I_2D/I_G ratio was 0.71, further affirming the presence of multilayered LIG [63].

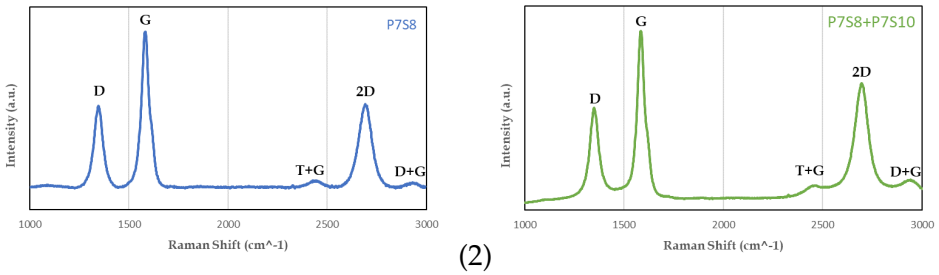

(1) (2)

Figure 5.3: Raman spectrum of LIG produced with (1) P7S8 and (2) P7S8+P7S10 laser parameters on the Whatman 1 substrate.

Measurements were taken for P6S6 and P7S8 laser parameters on the DLHC substrate. Figure 5.4 shows that both parameters do not indicate high quality fabrication. Although the LIG from P6S6 had three main peaks that were well-defined and sharp, the laser parameters P7S8 did not produce LIG with a pronounced 2D peak. For the P6S6 sample, in graph 5.4(1), the I_D/I_G ratio indicated a significant increase in carbon bond defects

when compared to the optimal performance parameters of the Whatman 1 paper substrate. At the same time, the I_2D/I_G ratio showed a value of 0.37 which is typical for material resembling multilayered graphene. This suggests the presence of a higher number of layers as compared to the previous substrate. The P7S8 sample, graph 5.4(2) displayed an I_D/I_G ratio above average, indicating an increased number of defects. Additionally, the I_2D/I_G ratio was low at 0.17, suggesting the formation of a high number of graphene layers during LIG formation.

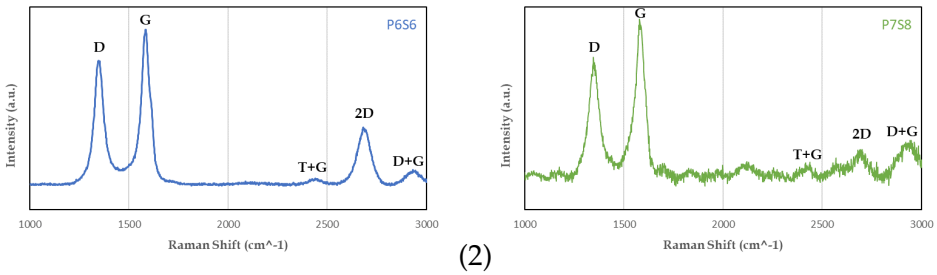

(1) (2)

Figure 5.4: Raman spectrum of LIG produced with (1) P6S6 and (2) P7S8 laser parameters on the DLHC cellulose substrate.

5.1.4 Morphological Characterization

To characterize the samples of LIG cellulose fibers from both substrates (DLHC and Whatman 1 paper sheets), SEM images were used. Morphological changes in the substrate such as surface fiber burning and graphene formation are expected. The SEM protocol was used for a selection of laser parameters based on the previous chemical and sheet resistance tests.

For the DLHC substrate, laser parameters P6S6 and P7S7 were chosen. In Figure 5.5 we can observe that the laser irradiation has a great impact on the cellulose fibers, mainly through ablation during LIG formation.

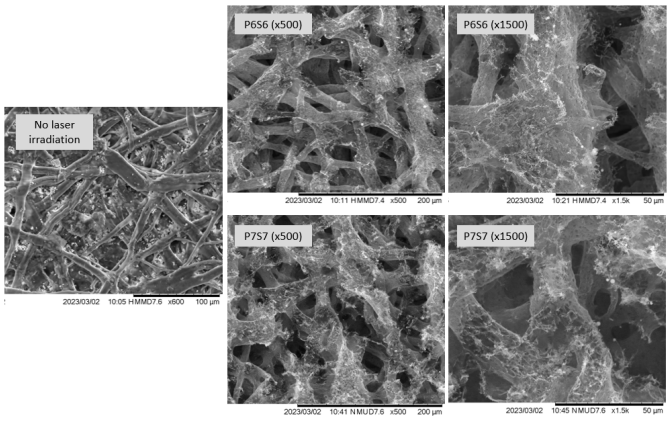

Figure 5.5: SEM images of DLHC substrate with no laser irradiation x600 (left) and after laser irradiation P6S6 (top) and P7S7 (bottom).Middle images with x500 and right images with x1500, magnification. Images taken at CENIMAT with Hitachi IM 3030Plus Tabletop Microscope.

This can be easily seen by comparing the image on the left, where there was no laser irradiation at magnification x600, with the images of the substrate after laser irradiation at magnification x500, which are in the center of Figure 5.5. The cellulose fibers lose their smoothness and compactness and become more jagged and porous. Comparing the images on the right, we can see that the upper right image (P6S6) looks less ragged and with less ablation due to the lower power than the lower right image (P7S7), which looks more ablated due to the higher energy, giving a more homogeneous LIG production. To find the best parameters for LIG production, it is necessary to compromise on the ablation in order to have a more continuous graphene network while reducing the porosity.

Only two laser parameters, P7S8 and a double pass variation of P7S8 + P7S10, were analyzed for the Whatman 1 paper substrate. The selection of these parameters was based on the findings from Pinheiro et al., where these laser performance showed good potential. The double pass variation was later recommended by supervisors, as recent studies conducted at CENIMAT [63] indicated its potential efficacy. Based on Figure 5.6, a distinction can be made between single and double pass irradiation techniques. The images at the top, using the single pass technique, reveal less ablation and fewer jagged edges compared to the double pass technique, which displays more degradation. The combination of these results and the sheet-resistance values suggest that the P7S8+P7S10 laser parameters produce a more conductive graphene due to a higher, yet not excessive ablation, resulting in a more uniform LIG formation. However, this technique has a drawback: the increase in porosity caused by the double-pass method can lead to capillary transport within the substrate during electrochemical testing, which ultimately creates a more fragile biosensor. This was confirmed in later stages of the experiment.

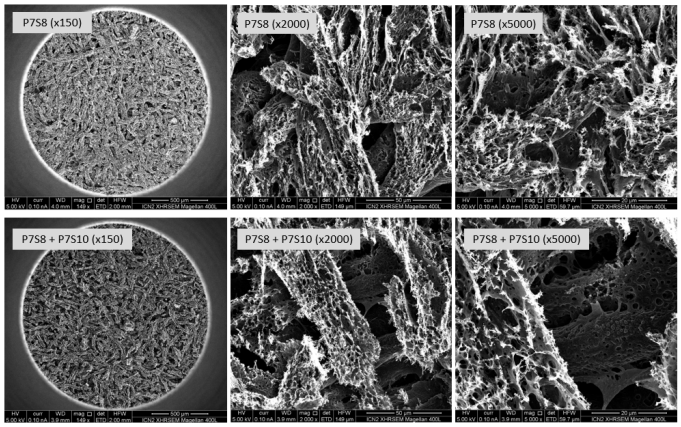

Figure 5.6: SEM images of Whatman 1 paper substrate and after single pass laser irradiation P7S8 (top) and double pass irradiation P7S8+P7S10 (bottom).Both parameters with images of x150 (left), x2000 (middle) and x5000 (right) magnitudes. Images taken at ICN2 with XHRSEM Magellan 400L Microscope.

5.1.5 Impermeability test of the DLHC substrate

To determine the effectiveness of the DLHC substrate in creating an electrochemical sensor, we conducted an impermeability test. We engraved several LIG squares on the substrate and added two droplets of MillQ water to visually assess hydrophobicity and impermeability. Unfortunately, the substrate did not pass the test as it absorbed all the water, rendering the LIG unusable. From Figure 5.7, it is evident that the substrate's two distinct cellulose layers, namely a top impermeable thin layer and a bottom permeable one, became disconnected once the bottom layer absorbed all the water. This phenomenon may be attributed to the laser irradiation that completely ablated the top layer because of its thin composition, resulting in the creation of LIG on the thicker bottom layer that has permeable properties. Based on our findings, we have concluded that it is not feasible to continue producing LIG electrodes using this innovative substrate.

Figure 5.7: Impermeability test for DLHC substrate.

5.1.6 Electrochemical Characterization

The final step in evaluating the performance of our LIG paper electrodes is electrochemical characterization. We will only employ the Whatman 1 paper substrate going forward as the DLHC substrate tests were not promising. The sensors designed for electrochemical characterization utilizing CV were produced using the P7S8 and P7S8+P7S10 laser parameters at z=-0.10in. The only difference between them was an increase in size of the counter electrode from the standard architecture in Pinheiro et al. (A1) to the second architecture (A2).

After sensor fabrication, both sensors were activated using KCl (0.1M) following the protocol described in section 4.4. The electrochemical performance was assessed through CV with an iron redox probe ($[Fe(CN)_6]^{3-}$]/[$Fe(CN)_6]^{4-}$] at 5mM, employing multiple scan rates (10, 25, 50, 100, and 150 mV s^{-1}). The purpose of this electrochemical characterization was to determine the optimal parameters and electrode architecture. Comparing P7S8 vs. P7S8+P7S10 and A1 vs. A2 allowed for the identification of the superior electrode architecture and optimal parameters.

Figure 5.8 shows the CV plots of multiple scan rates used to analyze the difference in electrode electrochemical performance of the P7S8 and P7S8+P7S10 laser settings. Only the fifth cycle of each scan rate is shown in the plots below.

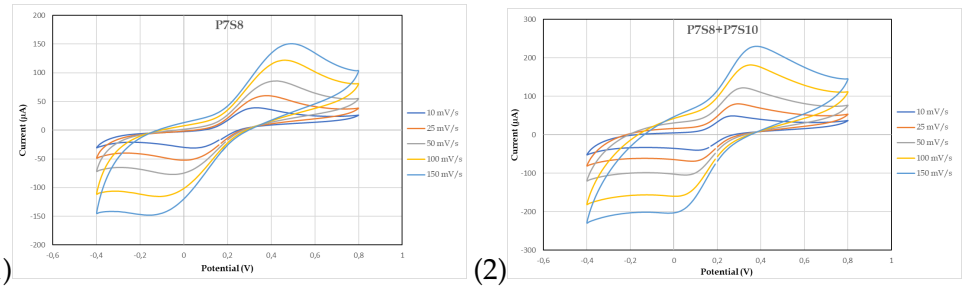

(1) (2)

Figure 5.8: CV plot of LIG produced with (1) P7S8 and (2) P7S8+P7S10 laser parameters (Whatman 1 paper substrate), using a ferri-ferrocyanide redox probe (5mM) for 10, 25, 50, 100, 150 mV s^{-1} scan rates.

Figure 5.8(1) shows the resulting CV for the P7S8 laser parameters, while Figure 5.8(2) shows the CV plots for the P7S8+P7S10 laser parameters. From the analysis of these plots, it is possible to see two distinct peaks, the cathodic (negative) peak resulting from the reduction of the iron probe and the anodic (positive) peak resulting from the oxidation of the iron probe, according to the IUPAC convention. These peaks can be seen for both of these specific samples, although they are more pronounced for the P7S8+P7S10, which is evidence that the electron transfer between the LIG surface and the iron redox probe is working, meaning that we have a well-functioning electrode. The scan rate study is performed for several increasing scan rates, so it is possible to see the dependence of Ip and peak separation (between anodic and cathodic peaks). As the scan rate increases, there is a tendency for both the anodic and cathodic peaks to have higher Ip and also the peak separation has a tendency to increase. This can be easily seen by looking at the plots in Figure 5.8. For the anodic peak in P7S8, the Ip increased from 40 to 150 µA, a difference of about 110 µA. The cathodic peak went from -30 to -150 µA, a difference of 120 µA. In terms of peak separation, it went from about 0.2 V at 10 mV s^{-1} to nearly 0.65 V at 150 mV s^{-1} scan rate. The anodic Ip in P7S8+P7S10 increased from about 40 to 225 µA, a difference of 185 µA. The cathodic peak went from -30 to -200 µA, a difference of 170 µA. In terms of peak separation, it went from about 0.2 V at 10 mV s^{-1} to almost 0.38 V at 150 mV s^{-1}. It is also noticeable an enlargement of the lower left part of the plots as the scan rate increases, after the cathodic peak, which is related to one of the limitations of the LIG sensors. Due to the porosity of the multilayered graphene, it acts as a capacitor so that the change transfer processes are not fully reversible.

For the anodic peak in P7S8 first architecture, the Ip increased from 100 to 480 µA, a difference of about 380 µA. The cathodic peak went from -80 to -440 µA, a difference of 360 µA, approximately. In terms of peak separation, it went from about 0.12 V at 10 mV s^{-1} to 0.34 V at 150 mV s^{-1} scan rate. The anodic Ip in P7S8 second architecture increased from about 70 to 330 µA, a difference of 260 µA. The cathodic peak went from -60 to -310 µA, a difference of 250 µA. In terms of peak separation, it went from about 0.14 V at 10 mV s^{-1} to almost 0.34 V at 150 mV s^{-1}.

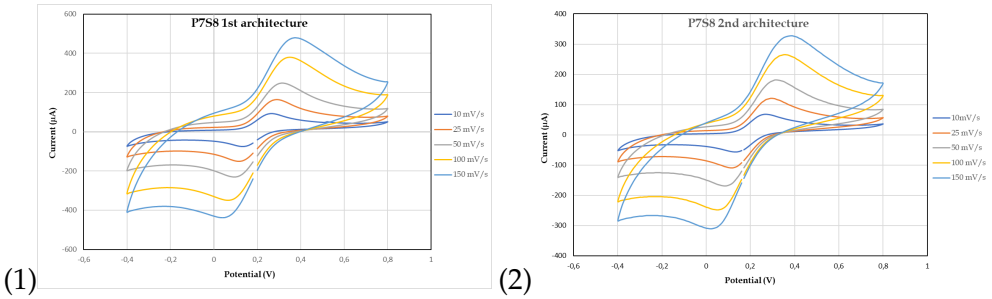

(1) (2)

Figure 5.9: CV plot of LIG produced with two different architectures, standard architecture on the left (1) and second architecture on the right (2), all with the P7S8 laser parameters (Whatman 1 paper substrate), using a ferri-ferrocyanide redox probe (5mM) for 10, 25, 50, 100, 150 mV s^{-1} scan rates.

Figure 5.10 illustrates the differences between the electrochemical behavior of LIG produced with two different laser parameters at a scan rate of 100 mV/s. There is an increase in peak current from the single pass to the double pass parameters as well as a decreased peak separation, which tells us that the double pass approach results in an electrode with more reversible electrochemical performance than its counterpart. In Figure 5.10, it can be seen that the first architecture has higher anodic and cathodic Ip at a scan rate of 100 mV s^{-1}, but in terms of peak separation, there isn't much difference, with both obtaining very similar peak separations.

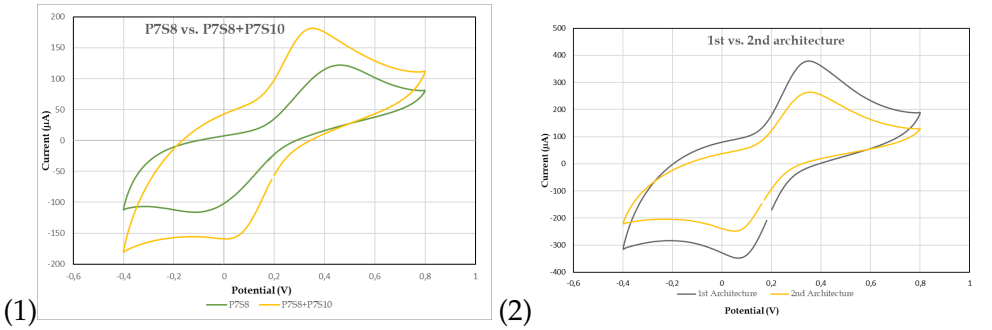

(1) (2)

Figure 5.10: CV plots. (1) Laser parameters comparison (2) Architecture comparison, against a ferri-ferrocyanide redox probe (5mM) for 100 mV s^{-1} scan rate.

5.1.6.1 Electrochemically Active Surface Area (ECSA) Determination

The ECSA is a very important parameter to consider when designing electrodes to analyze sensor performance. It gives us the effective surface area of an electrode that is available to interact with the analyte through electron transfer [65]. This parameter is closely related to the properties of the material, if the material used to fabricate the electrode is very porous, like LIG, it will have a much larger ECSA than other smoother materials.

To calculate the ECSA, we use the data collected by our CV analysis. We first average the anodic and cathodic Ip for each scan rate (5 cycles each) and then correlate them with the square root of each respective scan rate. We then construct a plot that shows this linear

correlation (Ip versus square root of each scan rate), resulting in the plots shown in Figure 5.11. The first (1) plots both laser parameters, and the second (2) plots both architectures.

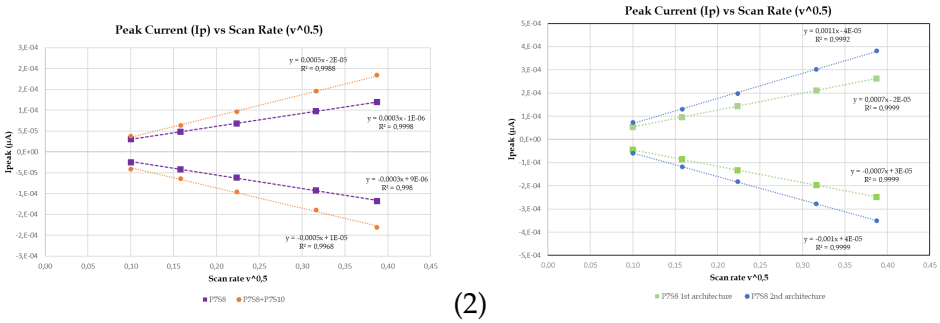

(1) (2)

Figure 5.11: Plots of the average cathodic and anodic Ip relative to the square root of the respective scan rates. (1) Laser parameters comparison (2) Architecture comparison.

Considering the Randles-Ševcik equation for quasi-reversible systems(equation A.1). And replacing the variables by the known constants, where Ip is the peak current, D is the diffusion coefficient of oxidation (6.7x10^{-6} cm^2 s^{-1}), C is the concentration of the redox probe (5x10^{-6} mol/cm3), n is the number of electrons participating in the reaction (n=1) and v is the scan rate. Associating it with the regression slope of the oxidation peak from the plots above (equation A.2).

By equalling I_p^{quasi} to I_p we obtain an expression (equation A.3) that can be used to determine the ECSA. Where the area (A) is a function of the slope (m). Calculating the results for the parameters in study, we obtained an ECSA of 0.09 cm^2 for the P7S8 parameters, an area of 0.15 cm^2 for the P7S8+P7S10 (double pass). The first and second architectures obtained areas of 0.31 cm^2 and 0.21 cm^2 respectively. These results imply that LIGs fabricated with two lasing cycles have a higher ECSA, and that the first architecture also has a higher ECSA compared to the second.

5.1.6.2 Heterogeneous Electron-transfer Rate (k^0) Determination

The k^0 is a crucial electrochemical characterization that offers insights into the speed of electron transfer between the analyte and electrode. These parameters are determinable using Nicholson and Lavagnini techniques. The determination is possible by employing CV, where the cathodic and anodic peak separations are considered for each scan rate and charted. The Lavagnini method then enables the determination of the kinetic parameter (ψ) as it is directly linked to peak separation by the equation A.4.

After converting the respective scanning rates to the inverse of their square root, we obtained the plots 5.12. By utilizing the Nicholson equation (ψ) (equation A.5), one can calculate the k^0.

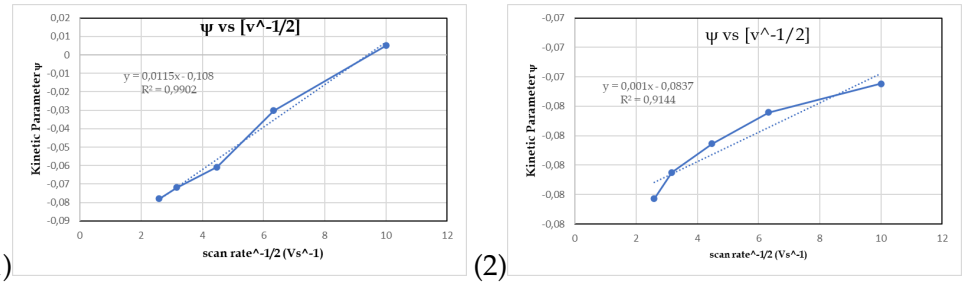

Figure 5.12: Plot of the dependency of the dimensionless kinetic parameter ψ on the applied scan rate for (1) P7S8 and (2) P7S8+P7S10 LIG.

To get the diffusion coefficients of the iron redox probes in KCL, we replaced D_0 ($7.2x10^{-6}cm^2s^{-1}$) and D_r ($6.7x10^{-6}cm^2s^{-1}$), and stipulated α as 0.5 due to symmetrical redox kinetics. This allowed us to obtain the simplified equation A.6.

Then k^0 can be calculated by using the corresponding slope value (m) from Figure 5.12 and inserting it into the equation A.7.

We obtained the k^0 values $3.3x10^{-4}cm\,s^{-1}$ and $2.9x10^{-5}cm\,s^{-1}$ from P7S8 and P7S8+P7S10, respectively. Based on our findings, it can be concluded that the P7S8 electrodes possess superior transfer charge properties compared to their double pass electrode counterpart.

5.2 Copper Detection Sensor

After optimizing the LIG fabrication, we chose the P7S8 laser parameters with the second architecture to fabricate all the LIG electrodes for this next stage, even though they were not the best electrochemically performing ones, for two main reasons. The first reason was that during testing we found that the electrodes fabricated with the double-pass laser were more fragile and broke more often. And the second reason was that in preliminary stripping anodic voltammetry tests, the second architecture actually produced higher SWASV peak currents than the first architecture. Therefore, all measurements in this section were performed with P7S8A2 electrodes.

The objective of this project is to create a practical and cost-efficient wearable biosensor prototype that collects biofluids such as sweat or urine to perform copper detection measurements. To obtain an optimal wearables device, we require a high-performing biosensor that is capable of detecting copper concentrations below the positive diagnostic threshold for WD, which is a Urinary Copper level of 100 µg/dL, or 1000 ppb according to [66], or a 24h Urinary Copper excretion between 40 and 100 µg/dL, a range of 400-1000 ppb according to [67]. This part of the project was developed at ICN2, Barcelona. Initially, the standard potential of regular LIG electrodes was determined using a set of SWASV testing various Cu concentrations (1000, 500, 200, 100, 50, 10, and 1 ppb Cu) referred to as the Drop Method. Next, the electrodes were subjected to optimal conditions for HM detection, where SWASV was performed with the electrode immersed in the solution with gentle agitation, intitled Immersion Method. Finally, we designed a microfluidic channel

to create a small and compact device that can simulate the agitation of biofluid solutions on the electrode surface using the Immersion Method, combined with the simplicity of the Drop Method, referred as the Microfluidics Method. The goal of this section is to be able to compare the results of the three methods, and to see the effect of the microfluidics in respect of the more standard methods.

5.2.1 Drop Method Testing

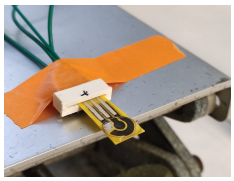

Figure 5.13: Example of the Drop Method setup.

The primary benefit of this method is its simplicity and ease of use. We utilized SWASV as an electrochemical method to investigate the electrodes analytical ability for HM. The previously formed LIG electrodes are activated using the procedure outlined in section 4.4. Taking the SWASV copper detection parameters from [50] as a starting point, we selected our own parameters for this electrochemical assessment. To deposit, we applied a -1 V potential for 60 seconds. Next, the equilibrium phase begins with a waiting time of 20 seconds during which no potential is applied to the solution. Following this, the stripping phase occurs, where we applied a potential range of -1 to 0.5 V with a 0.006 V potential step and 0.03 V in amplitude is applied at a frequency of 25 Hertz (Hz). Once the parameters are set up in the PalmSens software, a drop of 150 µL Copper Dissolution ([Cu]+AB) is applied to the sensor. The setup is then finalized, as shown in Figure 5.13. After performing this procedure for all the Copper concentrations and deducting the baseline (AB solution with no Copper), we acquired the plot 5.14(1). Visually, we can observe that the current peak related to copper should lie between the potentials of -0.3 and -0.1 V. To get a more detailed view, we magnified the graph in that particular region, resulting in the plot 5.14(2) that only exhibits the Cu peaks.

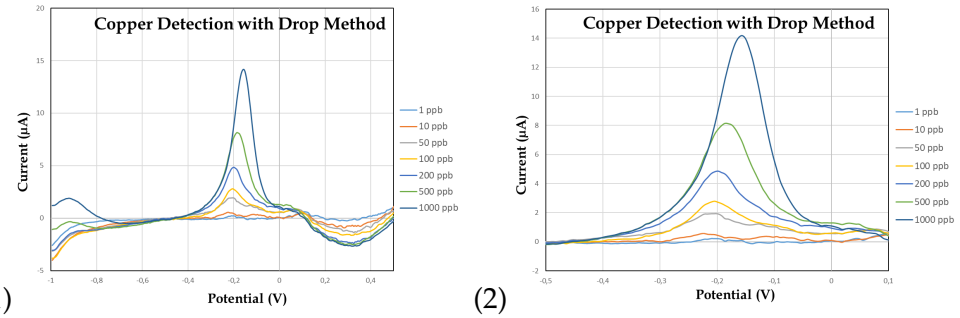

Figure 5.14: SWASV plots for the 1, 10, 50, 100, 200, 500 and 1000 ppb Copper concentrations. (1) Full curves SWASV after subtracting the AB baseline to remove the AB's influence. (2) A zoomed in prespective of the peaks located between -0.5 and -0.1 V.

5.2.1.1 Sensitivity and Limit of Detection Calculation

To calculate the Sensitivity, which is the rate of change of response per unit of analyte (µA/ppb), and LOD, which is the smallest analyte concentration reliably detectable in a sample [68], we compute the average peak current for every Copper concentration along with its standard deviation. This data is presented in the table 5.3.

Table 5.3: Average peak currents for all Copper concentrations and respective standard deviations, using the Drop Method.

[Cu] (ppb)	AB (0)	1	10	50	100	200	500	1000
Peak Curent (µA)	0,61	1,28	1,33	2,14	2,82	4,87	8,80	14,54
Strd	0,21	0,20	0,62	0,44	0,56	0,20	0,69	2,64

After creating a plot with the peak currents as a function of Cu concentration, we analyzed Figure 5.15(1) and traced a trend line to calculate its function. First we started by plotting the variables in a logaritmic scale, graph 5.15(1) so that only the Cu concentrations with a linear correlation are chosen to be linearly fitted as shown in plot 5.15(2).

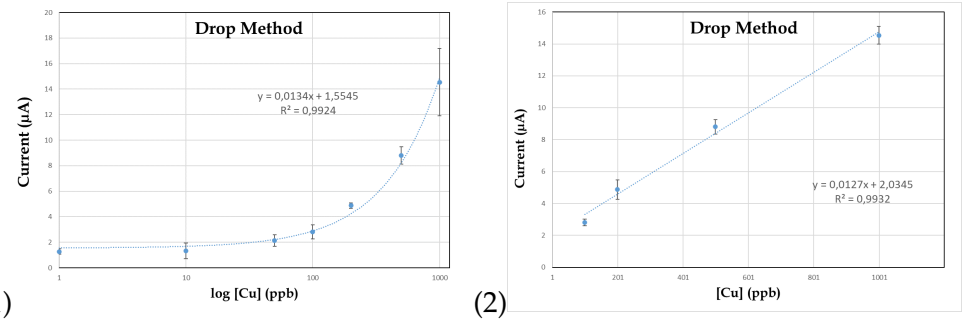

(1) (2)

Figure 5.15: (1) Plot of the peak curents (µA) in function of Copper concentration in logaritmic scale. (2) Plot of the last four concentrations peak curents (µA) in function of Copper concentration. Data points with the respective standard deviations and trend line for Drop Method.

From the linear regression of the above plot 5.15(1) we obtain the slope value (m) (0.0127 µA ppb^{-1}) and the b (2.03), and by calculating strd for the lowest Copper concentration sample (0.20 for 1ppm) we can calculate the LOD using the next equation 5.1:

$$LOD = \frac{([Cu]lowest + 3.3 * Strd[Cu]lowest - b)}{m} \tag{5.1}$$

The LOD obtained for the P7S8A2 electrodes with the drop method sense was 57.60 ppb which is a value well below the WD diagnostic concentration of 400 ppb, showing the potential of this system in this sense. The aim of this optimization is to obtain peaks with noticeable differences between each concentration in order to be able to quantify the copper concentration in the sample.

The system's sensitivity determines how much the signal changes between two concentrations. A higher sensitivity means that even a slight variation in concentration will

create significant signal changes. For this system the sensitivity was calculated from the slope value, obtaining a result of 0.0127 µA/ppb.

5.2.2 Immersion Method Testing

For the immersion method electrode test, a more elaborate and intricate system is necessary to ensure two main rules. The first concerns to the larger quantity of copper solution required, which requires a secure and stable method of submerging the electrode in the analyte solution. This obstacle was overcome by utilizing a laboratory elevator to handle the solution, and employing a lab support stand kit with a burette clamp to keep the electrode positioned as desired. During the SWASV deposition phase, the solution needs to be agitated. To meet this requirement, a Lab Magnetic Stirrer was placed on top of the Lab elevator. It could be turned on during the deposition phase and turned off during the Resting and Stripping phases of the SWASV protocol. All of this criterion was met and the final setup was design as Figure 5.16(1) portrays.

(1) 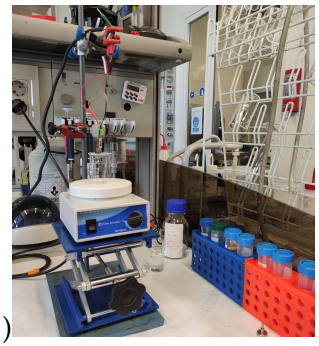 (2) 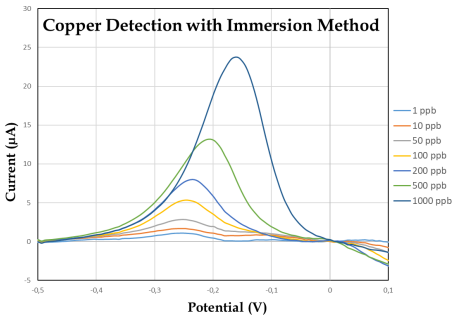

Figure 5.16: (1) Immersion Method setup. (2) SWASV plots for the 1, 10, 50, 100, 200, 500 and 1000 ppb Copper concentrations with Immersion Method.

From the electrochemical tests using SWASV, we obtained plot 5.16(2) by magnifying the Copper detection range between -0.3 and 0.1 V. All the peaks center at -0.2 V with a slight deviation towards the right as the copper concentration increases, proving that they are referencing to this specific HM.

5.2.2.1 Sensitivity and Limit of Detection

The computation of the average peak currents and their standard deviations for each concentration were calculated and displayed at the table 5.4.

Table 5.4: Average peak currents for all Copper concentrations and respective standard deviations, using the Immersion Method.

[Cu] (ppb)	0	1	10	50	100	200	500	1000
Peak Curent (µA)	0,49	1,17	2,54	4,29	5,69	8,41	13,42	23,90
Strd	0,09	0,66	0,10	0,04	1,49	1,60	1,59	6,69

The data was plotted on a logarithmic scale in order to determine the cutoff values for a reliable calibration curve, plot 5.17(1). The final five data points were chosen to create a plot of peak current against concentration, labeled as graph 5.17(2).

The sensitivity for this method is 0.0202 µA/ppb and the LOD 24.88 ppb. This setup achieved a lower LOD and higher sensitivity than the Drop Method, indicating an improvement in both metrics. This may be due to the higher volume of copper solution and the agitation of the solution in this setup which in turn allow more copper deposition on the electrode surface during the agitation phase of the SWASV protocol.

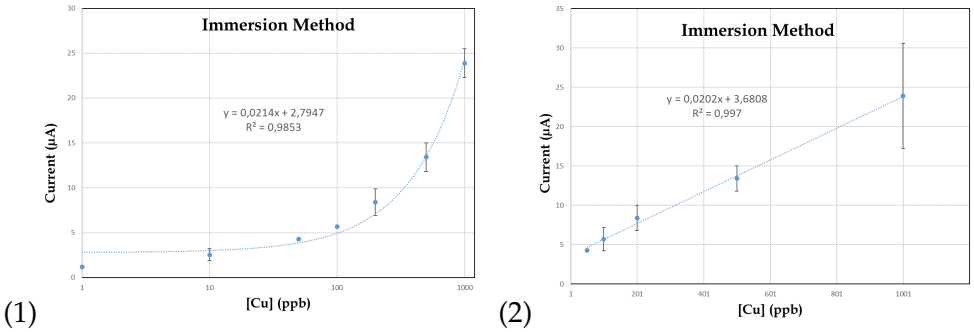

(1) (2)

Figure 5.17: (1) Plot of the peak curents (µA) in function of Copper concentration in logaritmic scale. (2) Plot of the last five concentrations peak curents (µA) in function of Copper concentration. Data points with the respective standard deviations and trend line.

5.2.3 Microfluidics Method Testing

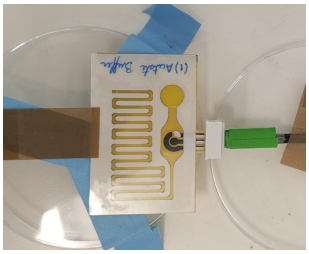

Figure 5.18: Example of the Microfluidics Method setup.

To create a compact and efficient device that mimics the fluid stirring of immersion methods, we devised a microfluidics channel that can be integrated with the LIG electrode. The ultimate aim of this design is to serve as a prototype for a wearable device in the future. In consideration of our goals, a microfluidics channel was designed with a three-minute flow time. This time was verified to provide a good amount of agitation in the microfluidics channel. We also adjusted the SWASV deposition time parameter to three minutes to ensure the flow is stopped during the SWASV resting phase. The resulting microfluidic channel is displayed in figure 5.18.

5.2.3.1 Microfluidics Channel

The microfluidics channel's design comprises of three distinct components. The top layer, made of PET, features laser cut inlets and outlets that play a crucial role in solution delivery and fluid flow inside the channel. This design allows air trapped inside the channel to escape when liquid is added, as illustrated in Figure 5.19(1). The design underwent testing and proved optimal for increasing flow. The inlet in the top layer is not a complete circle; it stops at 90% this allows the PET to hang slightly over the inlet, which facilitates the immediate entry of fluid into the channel. Additionally, the outlet is located further away from the inlet to prevent overflow from the inlet from covering the outlet and making the entire microfluidics channel unusable. This layer underwent an oxygen plasma treatment or a Ozone irradiation treatment to enhance its hydrophilicity, a critical step necessary for fluid flow in the microfluidic channel. Without this treatment, the thin channel would experience surface tension preventing flow. The middle layer, figure 5.19(2), consists of two bi-adhesive layers that are adhered to each other and subsequently laser cut into the shape of the channel. Our findings indicate that utilizing two layers produces superior flow performance due to the increased thickness of the channel which allows for more liquid volume to pass through. Upon analyzing the channel design, we can observe that the inlet area is a complete circle with the identical diameter as the inlet cutout in the previous layer. The chamber area is not cut in the shape of the electrode, but rather in a rectangular like shape with smooth edges which attach to the channel parts. This is critical for achieving a smooth and even filling of the chamber. Testing has shown that other shapes lead to the frequent presence of air bubbles inside the chamber. Additionally, the channel leading up to the chamber is twice as wide as the channel following the chamber. The purpose is to ensure a steady and rapid flow of fluid into the chamber, therefore improving the filling process. The channel was designed to optimize space efficiency, while still having sufficient material thickness between channel parts to allow for manual handling during device assembly. The third and final layer consists of an encapsulated electrode. A significant layer of wax surrounds the electrode to sufficiently fill the backside of the microfluidic device.

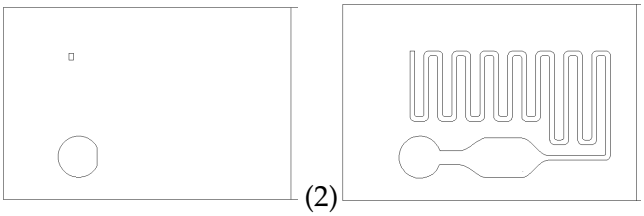

Figure 5.19: (1) PET layer AutoCad design. (2) Double Bi-adhesive layer AutoCad design.

During device assembly, it is necessary to take certain aspects into account. On occasion, the laser beam causes the PET layer's laser-cut borders to melt, requiring sanding before assembly with the rest of the device. This is critical for ensuring good adhesion between the two layers. Additionally, applying pressure to the device is crucial for achieving strong

adhesion. It was confirmed that localized pressure is often required to seal certain areas of the microfluidics and prevent fluid leakage.

5.2.3.2 Oxygen Plasma Cleaner

As discussed previously, hydrophilicity treatments on the PET plastic sheet used to cover the microfluidics channel are critical for optimal flow performance. One treatment method is placing the cut layers in a plasma chamber with the side that will be in contact with the channel facing up, followed by closing the plasma chamber and turning on the vacuum pump. The plasma chamber is activated and a controlled amount of oxygen is introduced by opening the valve until a bright purple hue is achieved. This process eliminates any organic contaminants, resulting in a clean surface that enhances wettability. After conducting tests to achieve a channel flow time of approximately 3 minutes (the time required for the complete flow of 150µL over the electrode), we found that 6 minutes produced an average time of 2 minutes and 38 seconds until the fluid reached the end of the channel and stopped. Once we optimized the time for the microfluidic channel, we conducted copper detection tests, resulting in obtaining the next SWASV curve peaks.

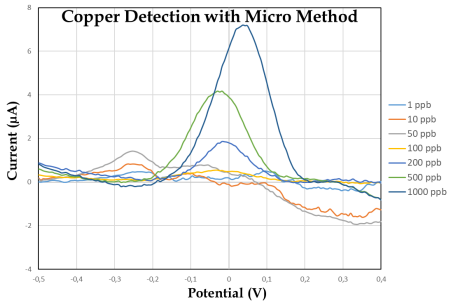

Figure 5.20: SWASV plots for the 1, 10, 50, 100, 200, 500 and 1000 ppb Copper concentrations with Microfluidics Method and Oxygen Plasma treatment.

Based on the results from the SWASV electrochemical test, we obtained plot XX, which reveals two peaks falling within the -0.3 to -0.2 V range for the 10 and 50 ppb Cu concentrations. However, since these peaks are not attributed to copper and may instead be related to the acetate buffer, they will not be taken into consideration for the subsequent analysis. The remaining peaks are found between -0.1 and -0.1 V and pertain to copper, rendering them suitable for calculating sensitivity and limit of detection.

Sensitivity and Limit of Detection The mean current value for every peak depicting different concentrations was calculated and exhibited in table 5.5.

Additionally, this data was utilized to obtain the two charts in figure 5.21. The first chart illustrates the data depicted in logarithmic scale, and from this chart, the points of the last three concentrations (200, 500, and 1000 ppb) were used to perform a linear fitting (as shown in figure 5.21(2)).

Table 5.5: Average peak currents for all Copper concentrations and respective standard deviations, using the Microfluidics Method with the Oxygen Plasma treatment.

[Cu] (ppb)	0	1	10	50	100	200	500	1000
Peak Curent (µA)	0,40	0,50	0,84	0,79	0,54	1,87	4,17	7,21
Strd	0,17	0,27	0,92	2,78	0,06	0,51	1,48	2,66

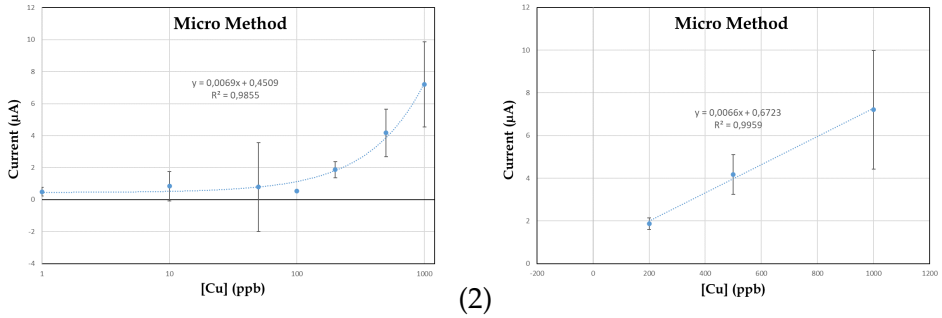

(1) (2)

Figure 5.21: (1) Plot of the peak curents (µA) in function of Copper concentration in logaritmic scale. (2) Plot of the last 3 concentrations peak curents (µA) in function of Copper concentration. Data points with the respective standard deviations and trend line.

The sensitivity for the Microfluidic Method with Oxygen treatment was 0.0066 µA/ppb, and the LOD was 42.44 ppb of copper. This represents a higher LOD compared to the Drop Method. Both methods had the same copper solution volume, suggesting that the fluid agitation in the microfluidics channel enhances the LOD. However, the sensitivity dropped by almost half despite the improved LOD, which suggests this system is worse at distinguishing copper solutions with close concentrations. Compared to the Immersion Method, there is a decrease in both LOD and sensitivity. This could be due to the reduced volume of copper solution or inadequate fluid agitation on the electrode surface caused by insufficient flow in the microfluidics channel.

5.2.3.3 Ozone Irradiation Cleaner

The oxygen plasma method of hydrophilizing the PET layer is highly dependent on manual control, as the user must constantly adjust the valve to maintain the bright purple color indicative of high-intensity oxygen plasma. Therefore, the treatment cannot be applied consistently. Given this, we tested the Ozone Irradiation technique, wherein a UV light is used to clean organic contaminants from the PET layers and leave a hydrophilic surface. Following the necessary tests to achieve a channel flow rate of 3 minutes, it was determined that the material should remain under the UV light for 15 minutes resulting in an average fluid flow time of 3 minutes and 7 seconds. This device operates independently meaning its less subjected to user error. Subsequently, copper detection tests utilizing SWASV were executed, and a magnified plot, 5.22, of the area of interest was obtained from the SWASV curves.

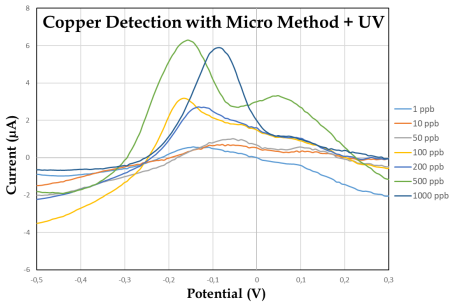

Figure 5.22: SWASV plots for the 1, 10, 50, 100, 200, 500 and 1000 ppb Copper concentrations with Microfluidics Method and Ozone Irradiation treatment.

Sensitivity and Limit of Detection The table 5.6 displays the mean peak current values for each concentration acquired via copper SWASV.

Table 5.6: Average peak currents for all Copper concentrations and respective standard deviations, using the Microfluidics Method with the UV/Ozone treatment.

[Cu] (ppb)	0	1	10	50	100	200	500	1000
Peak Curent (µA)	0,73	1,01	0,77	1,31	4,48	4,11	11,34	16,64
Strd	0,55	0,91	0,49	0,62	5,06	3,57	11,47	10,28

From these data points, two plots were generated in Figure 5.23. The last four points in the logarithmic scale of Graph 5.23(1) were used for linear fitting in Graph 5.23(2).

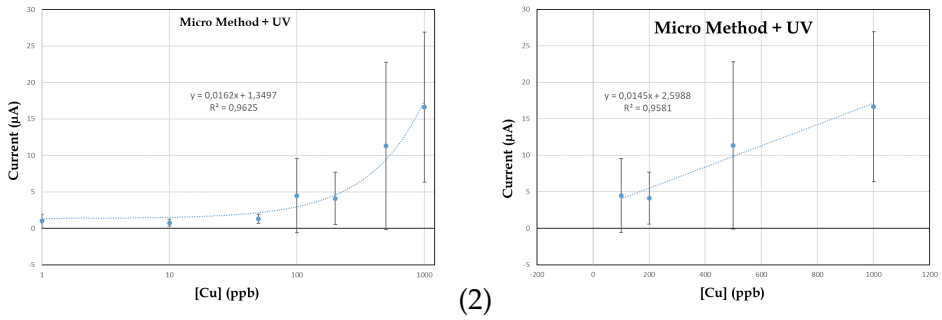

(1) (2)

Figure 5.23: (1) Plot of the peak curents (µA) in function of Copper concentration in logaritmic scale. (2) Plot of the last four concentrations peak curents (µA) in function of Copper concentration. Data points with the respective standard deviations and trend line.

The sensitivity for the Microfluidic Method with Ozone treatment was 0.0145 µA/ppb, and the LOD was 4.66 ppb of copper. The microfluidics technique utilizing ozone treatment improves both sensitivity and LOD as compared to the same technique utilizing oxygen plasma treatment. This may be due to a more stable and less user-dependent hydrophilization treatment than in its Oxygen Plasma chamber counterpart. Comparing this method with the Drop and Immersion methods, it is evident that it outperformed the Drop method in every aspect and demonstrated an improved LOD but lower sensitivity compared to the Immersion method. This represents a better overall performance compared to the other methods, but its variability must be taken into account.

6

Conclusions and Future work

The dissertation successfully met its goal by implementing LIG electrodes in a device that detects low copper concentrations to diagnose WD. This low-cost point-of-care solution for measuring copper in WD patients has the potential to save costs and resources for hospitals. The production of the electrode on a cellulose substrate (LIG on paper) indicates the possibility of a greener approach to medical devices.

Optimization tests were conducted on a DLHC substrate provided by AlmaScience. The optimization process involved conducting a series of systematic tests to identify the laser combinations that yield the best electrical, chemical, morphological and hydrophobic properties. To evaluate the correlation between laser power and speed, we carried out a preliminary test using a Power vs. Speed matrix. After conducting a visual analysis, it was determined that the optimal laser parameters for inducing graphene were those in which speed and power had similar values as any significant deviation resulted in either no graphene effect or ablation. Sheet-resistance tests demonstrated that the P6S6 and P7S7 parameters resulted in graphene with the lowest resistivities, with P6S6 presenting the lowest at 36.17 ± 1.06 Ω/sq. Raman spectroscopy assessed the chemical quality of the graphene produced by analyzing the I_D/I_G and I_{2D}/I_G ratios provided by the three characteristic graphene peaks. The electrodes fabricated with this substrate presented below average quality. We also used SEM analysis to analyze the physical effects of laser irradiation on the substrate. To conclude the research on the DLHC substrate, we conducted a wettability test to determine if the substrate remained hydrophobic after laser irradiation. However, the results indicated that this was not the case, as the water droplet was absorbed immediately. Therefore, it is not feasible to utilize this substrate for the production of electrochemical cells.

After conducting a literature review on LIG graphene electrodes on Whatman 1 paper that underwent wax treatment, we selected the P7S8 and P7S8+P7S10 laser parameters for further characterization of this substrate. The same set of characterization tests were made with the LIG produced with this substrate. Resistivity measurements indicate low resistivity, with a minimum of 9.68 ± 1.16 Ω sq^{-1}. Raman spectroscopy revealed a lower incidence of material defects, while the wax coating maintains substrate hydrophobicity even when submerged in water. To study the electrochemical capabilities of this substrate testing with CV scans to assess their ECSA and k^0. Two laser parameters were used: P7S8

vs. P7S8+P7S10. Additionally, we compared two different architectures, Architecture 1 vs. Architecture 2. The results reveal that the greatest ECSA was achieved with the laser double pass and Architecture 1, yielding 0.15 cm^2 and 0.31 cm^2 for the first architecture. The most effective electrode for k^0 was fabricated using a single pass laser method. Testing revealed that electrodes fabricated with a double pass laser method were significantly more fragile. Based on this, the optimization process for copper detection used P7S8 electrodes utilizing the second architecture.

To develop a point-of-care device we used three distinct methods. The first, named Drop Method, measured the efficacy of regular electrodes in copper detection systems. SWASV is a standard electrochemical test for HM detection, which we modified its parameters and reviewed for copper measurement. It was determined that the base electrodes can effectively detect copper at low concentrations - as low as 57.60 ppb Cu - with a sensitivity of 0.0127 µA/ppb. This value is bellow the minimum copper concentration necessary for diagnosing WD in patients. This setup is an easy way to measure copper but was proven quite unsafe because the sample solution is not contained, raising contaminations issues. Then we tested copper detection using a countertop method named Immersion Method, in this setup the biofluid is contained and agitation is added during the deposition phase of the SWASV protocol. Due to the electrode being submerged in a larger volume and the added agitation, copper could be detected at concentrations as low as 24.88 ppb Cu with a sensitivity of 0.0202 µA/ppb. This method exhibited excellent analytical performance but due to its requirement for a large setup and a significant amount of biofluid, it is not suitable for a point-of-care device. So, to overcome the flaws of this methods and combine their valences we proposed the Microfluidics Method. This method involves a custom-designed microfluidic channel where a drop of solution is placed on the inlet and biofluid runs through the channel, simulating the agitation aspect on top of the electrode. Two methods were utilized to hydrophilize the channel. The first involved using an Oxygen Plasma Chamber and resulted in devices capable of detecting concentrations as low as 42.44 ppb Cu with a sensitivity of 0.0066 µA/ppb. However, some inconsistencies in the oxygen cleaning process can occur. Therefore, we propose using the Microfluidic Method with an Ozone treatment to enhance hydrophilicity wich provided the capability of detecting copper at concentrations as low as 4.66 ppb, with a sensitivity of 0.0145 µA/ppb. This project led to the creation of a point-of-care device capable of WD diagnosis. The device's components are all laser engraved/cut, making production easy as every component is fabricated with the same machinery.

Overall, this dissertation presents a novel application of LIG electrodes that expands the field of sustainable biomedical devices. While this project shows promise for the development of a fully functioning and clinically tested device, there are still areas of improvement. For future work, tests with multi-HM solutions and with real sweat and urine samples should be conducted to assess its specificity and detection in real samples capability. In order to build a wearable device a sweat/urine collection system should also be considered.

Bibliography

[1] J. M. Lourenço. *The NOVAthesis LaTeX Template User's Manual*. NOVA University Lisbon. 2021. URL: https://github.com/joaomlourenco/novathesis/raw/main/template.pdf (cit. on p. i).

[2] P. Hedera. "Wilson's Disease: A Master of Disguise". In: *Parkinsonism amp;amp; Related Disorders* 59 (2019), pp. 140–145. DOI: 10.1016/j.parkreldis.2019.02.016 (cit. on p. 1).

[3] URL: https://medlineplus.gov/ency/article/000785.htm (cit. on p. 1).

[4] K.-H. Weiss and M. L. Schilsky. *Wilson disease: Pathogenesis, molecular mechanisms, diagnosis, treatment and monitoring*. Elsevier/Academic Press, 2019 (cit. on p. 1).

[5] P. Ferenci. "Pathophysiology and clinical features of Wilson Disease". In: *Metabolic Brain Disease* 19.3/4 (2004), pp. 229–239. DOI: 10.1023/b:mebr.0000043973.10494.85 (cit. on p. 1).

[6] H. Bradl. *Heavy metals in the environment: origin, interaction and remediation*. Elsevier, 2005 (cit. on p. 1).

[7] G. J. Brewer. "Recognition, diagnosis, and management of Wilson's Disease". In: *Proceedings of the Society for Experimental Biology and Medicine* 223.1 (2000), pp. 39–46. DOI: 10.1046/j.1525-1373.2000.22305.x (cit. on p. 1).

[8] E. A. Roberts and M. L. Schilsky. "Diagnosis and treatment of Wilson Disease: An update". In: *Hepatology* 47.6 (2008), pp. 2089–2111. DOI: 10.1002/hep.22261 (cit. on p. 1).

[9] P. Ferenci et al. "Diagnosis and phenotypic classification of Wilson disease1". In: *Liver International* 23.3 (2003), pp. 139–142. DOI: 10.1034/j.1600-0676.2003.00824.x (cit. on p. 1).

[10] J.-B. Tu and R. Blackwell. "Studies on levels of penicillamine-induced cupriuresis in heterozygotes of Wilson's disease". In: *Metabolism* 16.6 (1967), pp. 507–513. DOI: 10.1016/0026-0495(67)90079-0 (cit. on p. 2).

[11] C. S. Palumbo and M. L. Schilsky. "Clinical practice guidelines in Wilson Disease". In: *Annals of Translational Medicine* 7.S2 (2019). DOI: 10.21037/atm.2018.12.53 (cit. on p. 2).

[12] E. A. Roberts and M. L. Schilsky. "Diagnosis and treatment of Wilson Disease: An update". In: *Hepatology* 47.6 (2008), pp. 2089–2111. DOI: 10.1002/hep.22261 (cit. on p. 2).

[13] A. Poujois and F. Woimant. "Wilson's Disease: A 2017 update". In: *Clinics and Research in Hepatology and Gastroenterology* 42.6 (2018), pp. 512–520. DOI: 10.1016/j.clinre.2018.03.007 (cit. on p. 2).

[14] S. Jeong et al. "Laser-induced graphene incorporated with silver nanoparticles applied for heavy metal multi-detection". In: *Journal of Materials Chemistry A* 11.25 (2023), pp. 13409–13418. DOI: 10.1039/d3ta00691c (cit. on p. 2).

[15] S. P. Singh et al. "Sulfur-doped laser-induced porous graphene derived from polysulfone-class polymers and membranes". In: *ACS Nano* 12.1 (2017), pp. 289–297. DOI: 10.1021/acsnano.7b06263 (cit. on p. 2).

[16] R. Qin et al. "Flexible fabrication of flexible electronics: A general laser ablation strategy for robust large-area copper-based electronics". In: *Advanced Electronic Materials* 5.10 (2019), p. 1900365. DOI: 10.1002/aelm.201900365 (cit. on p. 2).

[17] R. Martins, I. Ferreira, and E. Fortunato. "Electronics with and on paper". In: *physica status solidi (RRL) - Rapid Research Letters* 5.9 (2011), pp. 332–335. DOI: 10.1002/pssr.201105247 (cit. on p. 2).

[18] Y. Chyan et al. "Laser-induced graphene by multiple lasing: Toward electronics on cloth, paper, and food". In: *ACS Nano* 12.3 (2018), pp. 2176–2183. DOI: 10.1021/acsnano.7b08539 (cit. on pp. 2, 9).

[19] P. T. Kissinger. "Biosensors—a perspective". In: *Biosensors and Bioelectronics* 20.12 (2005), pp. 2512–2516. DOI: 10.1016/j.bios.2004.10.004 (cit. on p. 4).

[20] D. R. Thevenot et al. "Electrochemical biosensors: Recommended definitions and classification". In: *Pure and Applied Chemistry* 71.12 (1999), pp. 2333–2348. DOI: 10.1351/pac199971122333 (cit. on p. 4).

[21] J. Wang. "Glucose Biosensors: 40 Years of Advances and Challenges". In: *Electroanalysis* 13.12 (2001), pp. 983–988. DOI: 10.1002/1521-4109(200108)13:12<983::aid-elan983>3.0.co;2-# (cit. on p. 4).

[22] N. J. Ronkainen, H. B. Halsall, and W. R. Heineman. "Electrochemical biosensors". In: *Chemical Society Reviews* 39.5 (2010), p. 1747. DOI: 10.1039/b714449k (cit. on p. 4).

[23] D. Grieshaber et al. "Electrochemical biosensors - sensor principles and Architectures". In: *Sensors* 8.3 (2008), pp. 1400–1458. DOI: 10.3390/s80314000 (cit. on pp. 5, 9).

[24] E. B. Bahadır and M. K. Sezgintürk. "Applications of graphene in electrochemical sensing and biosensing". In: *TrAC Trends in Analytical Chemistry* 76 (2016), pp. 1–14. DOI: 10.1016/j.trac.2015.07.008 (cit. on p. 5).

[25] S. K. Tiwari et al. "Graphene research and their outputs: Status and Prospect". In: *Journal of Science: Advanced Materials and Devices* 5.1 (2020), pp. 10–29. DOI: 10.1016/j.jsamd.2020.01.006 (cit. on p. 5).

[26] URL: https://www.sciencedirect.com/book/9780444519580/handbook-of-electrochemistry (cit. on p. 5).

[27] B. D. A. C. *Handbook of Graphene Electrochemistry*. SPRINGER, 2016 (cit. on p. 5).

[28] P. T. Kissinger and W. R. Heineman. "Cyclic voltammetry". In: *Journal of Chemical Education* 60.9 (1983), p. 702. DOI: 10.1021/ed060p702 (cit. on p. 6).

[29] URL: https://www.ossila.com/en-eu/pages/cyclic-voltammetry-applications (cit. on p. 6).

[30] Q. Yang et al. "Development of a Heavy Metal Sensing Boat for Automatic Analysis in Natural Waters Utilizing Anodic Stripping Voltammetry". In: *ACS ESamp;amp;T Water* 1.12 (2021), pp. 2470–2476. DOI: 10.1021/acsestwater.1c00192 (cit. on pp. 6, 12).

[31] A. M. Santos et al. "Square-wave adsorptive anodic stripping voltammetric determination of norfloxacin using a glassy carbon electrode modified with carbon black and CdTe quantum dots in a chitosan film". In: *Microchimica Acta* 186.3 (2019). DOI: 10.1007/s00604-019-3268-1 (cit. on pp. 6, 7).

[32] B. J. Feldman et al. "Determination of Lead in Blood by Square Wave Anodic Stripping Voltammetry at a Carbon Disk Ultramicroelectrode". In: *Analytical Chemistry* 66.13 (1994), pp. 1983–1987. DOI: 10.1021/ac00085a010 (cit. on p. 7).

[33] Y. Fang and E. Wang. "Electrochemical biosensors on platforms of graphene". In: *Chemical Communications* 49.83 (2013), p. 9526. DOI: 10.1039/c3cc44735a (cit. on p. 7).

[34] A. K. Geim. "Graphene: Status and prospects". In: *Science* 324.5934 (2009), pp. 1530–1534. DOI: 10.1126/science.1158877 (cit. on p. 7).

[35] A. K. Geim and K. S. Novoselov. "The rise of graphene". In: *Nature Materials* 6.3 (2007), pp. 183–191. DOI: 10.1038/nmat1849 (cit. on p. 7).

[36] K. S. Novoselov et al. "Electric field effect in atomically thin carbon films". In: *Science* 306.5696 (2004), pp. 666–669. DOI: 10.1126/science.1102896 (cit. on p. 7).

[37] K. S. Novoselov et al. "A roadmap for graphene". In: *Nature* 490.7419 (2012), pp. 192–200. DOI: 10.1038/nature11458 (cit. on p. 7).

[38] W. Ma et al. "Recent advances in preparation and application of laser-induced graphene in energy storage devices". In: *Materials Today Energy* 18 (2020), p. 100569. DOI: 10.1016/j.mtener.2020.100569 (cit. on pp. 7, 10).

[39] Z. Wan et al. "Laser induced graphene for biosensors". In: *Sustainable Materials and Technologies* 25 (2020). DOI: 10.1016/j.susmat.2020.e00205 (cit. on pp. 7, 10).

[40] L. Cao et al. "Stable and durable laser-induced graphene patterns embedded in polymer substrates". In: *Carbon* 163 (2020), pp. 85–94. DOI: 10.1016/j.carbon.2020.03.015 (cit. on pp. 7, 10).

[41] H. Liu and Y. Chen. "Laser-induced graphene film and its applications in Flexible Electronics". In: *Applied Sciences* 12.21 (2022), p. 11233. DOI: 10.3390/app122111233 (cit. on pp. 7, 8).

[42] L. Huang et al. "Laser-induced graphene: En route to Smart Sensing". In: *Nano-Micro Letters* 12.1 (2020). DOI: 10.1007/s40820-020-00496-0 (cit. on pp. 7, 8).

[43] T. Pinheiro et al. "Influence of CO2 laser beam modelling on electronic and electrochemical properties of paper-based laser-induced graphene for disposable ph electrochemical sensors". In: *Carbon Trends* 11 (2023), p. 100271. DOI: 10.1016/j.cartre.2023.100271 (cit. on p. 8).

[44] T. Pinheiro et al. "Laser-induced graphene on paper toward efficient fabrication of flexible, planar electrodes for electrochemical sensing". In: *Advanced Materials Interfaces* 8.22 (2021). DOI: 10.1002/admi.202101502 (cit. on pp. 9–11, 21).

[45] H. A. Abdulbari and E. A. Basheer. "Electrochemical biosensors: Electrode Development, materials, design, and fabrication". In: *ChemBioEng Reviews* 4.2 (2017), pp. 92–105. DOI: 10.1002/cben.201600009 (cit. on p. 10).

[46] J. Lin et al. "Laser-induced porous graphene films from commercial polymers". In: *Nature Communications* 5.1 (2014). DOI: 10.1038/ncomms6714 (cit. on pp. 10, 23).

[47] I. Cretescu et al. "Electrochemical sensors for heavy metal ions detection from Aqueous Solutions". In: *Environmental Engineering and Management Journal* 11.2 (2012), pp. 463–470. DOI: 10.30638/eemj.2012.058 (cit. on p. 11).

[48] L. Pujol et al. "Electrochemical sensors and devices for heavy metals assay in water: The French groups' contribution". In: *Frontiers in Chemistry* 2 (2014). DOI: 10.3389/fchem.2014.00019 (cit. on p. 11).

[49] M. Lin et al. "Electrochemical detection of copper ion using a modified copolythiophene electrode". In: *Electrochimica Acta* 54.27 (2009), pp. 7012–7017. DOI: 10.1016/j.electacta.2009.07.025 (cit. on p. 11).

[50] Q. Yang et al. "Wearable and fully printed microfluidic nanosensor for sweat rate, conductivity, and copper detection with healthcare applications". In: *Biosensors and Bioelectronics* 202 (2022), p. 114005. DOI: 10.1016/j.bios.2022.114005 (cit. on pp. 12, 31).

[51] 2015-01. URL: https://www.manualslib.com/manual/827813/Universal-Laser-Systems-Vls2-30.html (cit. on p. 14).

[52] M. Ramasamy and J. W. Ha. "Influence of oxygen plasma treatment on structural and spectral changes in gold nanorods immobilized on indium tin oxide surfaces". In: *The Journal of Chemical Physics* 157.1 (2022). DOI: 10.1063/5.0097220 (cit. on p. 14).

[53] B. Jiang et al. "Oxygen Plasma Modified Carbon Cloth with C=O Zincophilic Sites as a Stable Host for Zinc Metal Anodes". In: *Frontiers in Chemistry* 10 (2022). DOI: 10.3389/fchem.2022.899810 (cit. on p. 14).

[54] K. Bazaka et al. "Oxygen plasmas: a sharp chisel and handy trowel for nanofabrication". In: *Nanoscale* 10.37 (2018), pp. 17494–17511. DOI: 10.1039/c8nr06502k (cit. on p. 14).

[55] Fct/unl. *Biorad/Nanometrics HL5500 Hall effect systems*. URL: https://www.cenimat.fct.unl.pt/lab-facilities/electrical-characterization-lab/biorad/nanometrics-hl5500-hall-effect-systems (cit. on p. 15).

[56] F. Keywell and G. Dorosheski. "Measurement of the Sheet Resistivity of a Square Wafer with a Square Four-Point Probe". In: *Review of Scientific Instruments* 31.8 (1960), pp. 833–837. DOI: 10.1063/1.1717065 (cit. on p. 15).

[57] R. R. Jones et al. "Raman Techniques: Fundamentals and Frontiers". In: *Nanoscale Research Letters* 14.1 (2019). DOI: 10.1186/s11671-019-3039-2 (cit. on p. 15).

[58] S. Zhang et al. "Molecular Fingerprint Detection Using Raman and Infrared Spectroscopy Technologies for Cancer Detection: A Progress Review". In: *Biosensors* 13.5 (2023), p. 557. DOI: 10.3390/bios13050557 (cit. on p. 15).

[59] A. Ul-Hamid. In: *A Beginners' Guide to Scanning Electron Microscopy* (2018). DOI: 10.1007/978-3-319-98482-7 (cit. on p. 15).

[60] K. Vernon-Parry. "Scanning electron microscopy: an introduction". In: *III-Vs Review* 13.4 (2000), pp. 40–44. DOI: 10.1016/s0961-1290(00)80006-x (cit. on p. 15).

[61] 2023-07. URL: https://www.palmsens.com/potentiostat/ (cit. on p. 16).

[62] A. W. Colburn et al. "Lifting the lid on the potentiostat: a beginner's guide to understanding electrochemical circuitry and practical operation". In: *Physical Chemistry Chemical Physics* 23.14 (2021), pp. 8100–8117. DOI: 10.1039/d1cp00661d (cit. on p. 16).

[63] A. Samouco et al. "Laser-induced electrodes towards low-cost flexible UV ZnO sensors". In: *Flexible and Printed Electronics* 3.4 (2018), p. 044002. DOI: 10.1088/2058-8585/aaed77 (cit. on pp. 23, 25).

[64] R. Murray et al. "Design of Experiments and Optimization of Laser-Induced Graphene". In: *ACS Omega* 6.26 (2021), pp. 16736–16743. DOI: 10.1021/acsomega.1c00309 (cit. on p. 23).

[65] P. Zhu and Y. Zhao. "Cyclic voltammetry measurements of electroactive surface area of porous nickel: Peak current and peak charge methods and diffusion layer effect". In: *Materials Chemistry and Physics* 233 (2019), pp. 60–67. DOI: 10.1016/j.matchemphys.2019.05.034 (cit. on p. 28).

[66] H. S. Chaudhry and A. C. Anilkumar. "Wilson Disease". In: *StatPearls*. StatPearls Publishing, 2023 (cit. on p. 30).

[67] M. Patil et al. "A review and current perspective on Wilson disease". In: *Journal of Clinical and Experimental Hepatology* 3.4 (2013), pp. 321–336. DOI: 10.1016/j.jceh.2013.06.002 (cit. on p. 30).

[68] A. Shrivastava and V. Gupta. "Methods for the determination of limit of detection and limit of quantitation of the analytical methods". In: *Chronicles of Young Scientists* 2.1 (2011), p. 21. DOI: 10.4103/2229-5186.79345 (cit. on p. 32).

A

Appendix

A.1 Figures

(1) 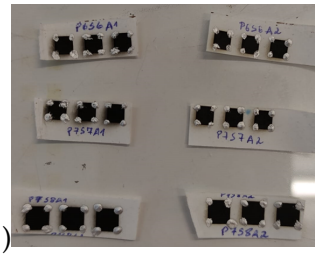 (2) 

Figure A.1: Sheet-Resistance setup for (1) AlmaScience substrate and (2) Whatman 1 substrate.

A.2 Equations

$$I_p^{quasi} = 0.436nFA_eC\sqrt{\frac{nFDv}{RT}} \tag{A.1}$$

$$I_p = mv^{1/2} \tag{A.2}$$

$$A = \frac{m}{3.99x10^{-3}} \tag{A.3}$$

$$\psi = \frac{-0.6288 + 0.021x}{1 - 0.017x} \tag{A.4}$$

$$\psi = k^0(\frac{D_0}{D_r})\frac{\alpha}{2}\sqrt{\frac{RT}{\pi nFD_0v}} \tag{A.5}$$

$$\psi = 34.194k^0v^{-\frac{1}{2}} \tag{A.6}$$

$$k^0 = \frac{m}{34.195} \tag{A.7}$$